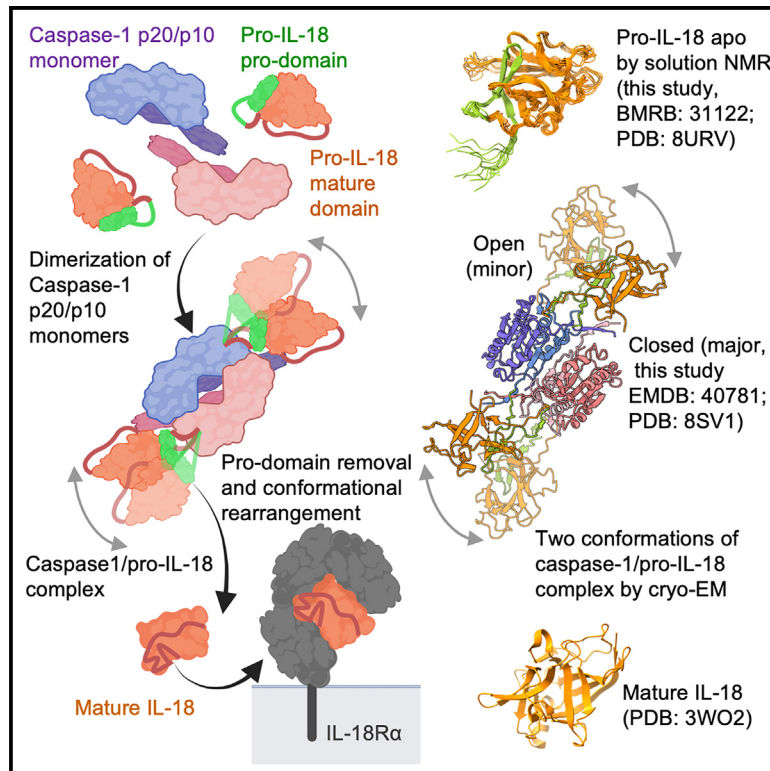


Structural transitions enable interleukin-18 maturation and signaling

Graphical abstract



Authors

Ying Dong, Jeffrey P. Bonin, Pascal Devant, ..., Jonathan C. Kagan, Lewis E. Kay, Hao Wu

Correspondence

jonathan.kagan@childrens.harvard.edu (J.C.K.),
lewis.kay@utoronto.ca (L.E.K.),
wu@crystal.harvard.edu (H.W.)

In brief

The inflammatory activity of IL-1 family cytokines is unleashed by caspase cleavage, but the underlying molecular mechanisms are unclear. Here, using cryo-EM and NMR techniques, Dong et al. reveal the conformational steps in the pathway for recognition and cleavage of pro-IL-18 by caspase-1 and suggest diverse ways with which inflammatory caspases process their substrates.

Highlights

- Cryo-EM structure reveals two major conformations of the caspase-1/pro-IL-18 complex
- Caspase-1 cleavage of pro-IL-18 depends less on the exosite interaction than caspase-4
- NMR structure of apo pro-IL-18 is similar to that of caspase-1-bound pro-IL-18
- The receptor-binding site of IL-18 is built by conformational changes upon cleavage

Article

Structural transitions enable interleukin-18 maturation and signaling

Ying Dong,^{1,2,9} Jeffrey P. Bonin,^{3,4,5,9} Pascal Devant,^{6,9} Zhuoyi Liang,^{7,9} Alexander I.M. Sever,^{4,5} Julian Mintseris,⁸ James M. Aramini,^{3,4,5} Gang Du,^{1,2} Stephen P. Gygi,⁸ Jonathan C. Kagan,^{6,*} Lewis E. Kay,^{3,4,5,*} and Hao Wu^{1,2,10,*}

¹Department of Biological Chemistry and Molecular Pharmacology, Harvard Medical School, Boston, MA, USA

²Program in Cellular and Molecular Medicine, Boston Children's Hospital, Boston, MA, USA

³Departments of Molecular Genetics and Biochemistry, University of Toronto, Toronto, ON M5S 1A8, Canada

⁴Department of Chemistry, University of Toronto, Toronto, ON M5S 3H6, Canada

⁵Program in Molecular Medicine, The Hospital for Sick Children Research Institute, Toronto, ON M5G 0A4, Canada

⁶Division of Gastroenterology, Boston Children's Hospital, Harvard Medical School, Boston, MA, USA

⁷Bioscience and Biomedical Engineering Thrust, Brain and Intelligence Research Institute, The Hong Kong University of Science and Technology (Guangzhou), Guangzhou, China

⁸Department of Cell Biology, Harvard Medical School, Harvard University, Boston, MA, USA

⁹These authors contributed equally

¹⁰Lead contact

*Correspondence: jonathan.kagan@childrens.harvard.edu (J.C.K.), lewis.kay@utoronto.ca (L.E.K.), wu@crystal.harvard.edu (H.W.)

<https://doi.org/10.1016/j.immuni.2024.04.015>

SUMMARY

Several interleukin-1 (IL-1) family members, including IL-1 β and IL-18, require processing by inflammasome-associated caspases to unleash their activities. Here, we unveil, by cryoelectron microscopy (cryo-EM), two major conformations of the complex between caspase-1 and pro-IL-18. One conformation is similar to the complex of caspase-4 and pro-IL-18, with interactions at both the active site and an exosite (closed conformation), and the other only contains interactions at the active site (open conformation). Thus, pro-IL-18 recruitment and processing by caspase-1 is less dependent on the exosite than the active site, unlike caspase-4. Structure determination by nuclear magnetic resonance uncovers a compact fold of apo pro-IL-18, which is similar to caspase-1-bound pro-IL-18 but distinct from cleaved IL-18. Binding sites for IL-18 receptor and IL-18 binding protein are only formed upon conformational changes after pro-IL-18 cleavage. These studies show how pro-IL-18 is selected as a caspase-1 substrate, and why cleavage is necessary for its inflammatory activity.

INTRODUCTION

Members of the interleukin-1 (IL-1) cytokine family play central roles in providing host protection in response to infection and tissue damage.^{1–5} In resting cells, several members of this cytokine family are expressed as inactive pro-forms in the cytosol, with an N-terminal prodomain and a C-terminal mature domain. Proteolytic cleavage of the IL-1 family members occurs at the junction between the two domains at sites marked by specific tetrapeptide sequences (P1–P4) and is commonly mediated by inflammatory caspases.^{6,7} The biological activities of these cytokines are achieved when the prodomains are removed and the mature chains are released to the outside of the cells through gasdermin D (GSDMD) pores or by way of membrane rupture during pyroptosis, a lytic form of cell death.^{8–14} The released cytokines amplify the immune response by binding to their receptors on the same cells and neighboring cells.¹ Why the prodomains need to be removed from IL-1 family cytokines to unleash their signaling capacities is unknown, but it is most commonly believed that the prodomains are disordered and prevent receptor binding by steric hindrance.¹⁵

The inflammatory caspases include caspase-1, 4, and 5 in humans and caspase-1 and 11 in mice.^{16,17} These caspases consist of an N-terminal caspase recruitment domain (CARD) and a C-terminal catalytic domain and are expressed as inactive zymogens. During canonical inflammasome activation, caspase-1 CARD filaments are formed,¹⁸ promoting molecular proximity of the catalytic domain and enhancing the kinetics of substrate-induced dimerization,¹⁹ resulting in the enhancement of caspase-1 enzymatic activity and auto-processing to gain substrate-cleavage activity. Caspase-4, 5, and 11, by contrast, are activated upon binding lipopolysaccharides (LPS) from bacteria.²⁰ Auto-processing of caspases occurs at specific sites at the interdomain linker (IDL) between the large (~20–22 kDa) and small subunits (~10–12 kDa) of the catalytic domain, as well as at the CARD linker (CDL) between the CARD and the large subunit of the catalytic domain.²¹ IDL processing is required to achieve protease activity toward various substrates.^{6,17,21}

All inflammatory caspases cleave GSDMD to stimulate its pore-forming activities, but they differ in their cytokine cleavage profiles. Caspase-4, 5, and 11 were initially reported to only

process GSDMD,^{9,10} but later studies revealed that caspase-4 and 5, but not caspase-11, also efficiently cleave pro-IL-18²² and weakly cleave pro-IL-1 β .^{23,24} We and others have recently reported the structure of the caspase-4/pro-IL-18 complex, which reveals a mode of interaction that relies on interaction at the active site as well as an exosite.^{25,26} In comparison with caspase-4, caspase-1 adopts a broader range of substrate-cleavage activity, including pro-IL-1 β , pro-IL-18, and pro-IL-37.^{27–32}

In this study, we made further strides in establishing the molecular mechanisms for the IL-18 maturation pathway and identified important differences in pro-IL-18 processing by caspase-1 relative to caspase-4. We first characterized the substrate-cleavage specificity of human caspase-1 and revealed that auto-processing of caspase-1 at D297 and D316 of the IDL to form the 20 kDa (p20) and 10 kDa (p10) subunits is required for caspase-1 to attain efficient substrate-cleavage activity on pro-IL-18 and pro-IL-1 β . We then captured a stable complex between the caspase-1 catalytic mutant (C285A) and pro-IL-18 and determined its cryoelectron microscopy (cryo-EM) structure. The structure determination revealed two major conformations, one similar to that observed in the caspase-4/pro-IL-18 structure,^{25,26} and one not dependent on the exosite interaction. We validated that the exosite was less important for pro-IL-18 processing by caspase-1 than by caspase-4, illustrating a notable distinction between the two caspases and explaining the wider substrate spectrum of caspase-1. Finally, we determined the structure of apo pro-IL-18 by nuclear magnetic resonance (NMR) spectroscopy, which revealed a compact structure with only local conformational differences from pro-IL-18 in complex with caspase-1. However, the pro-IL-18 structure in the apo or the caspase-1-bound state exhibits extensive conformational differences with the mature IL-18 structure, illustrating how IL-18 refolds upon cleavage to build its binding sites for the IL-18 receptor and the IL-18 binding protein (IL-18BP) to induce signaling and regulation.

RESULTS

Caspase-1 cleaves different substrates and forms a stable complex with pro-IL-18

We confirmed that caspase-1 is the major effector enzyme responsible for pyroptosis and IL-1 cytokine cleavage downstream of canonical inflammasome activation in human cells. Non-target single guide RNA (sgRNA)-treated human THP-1 macrophages primed with LPS and stimulated with the NOD-, LRR-, and pyrin domain-containing protein 3 (NLRP3) activator nigericin released IL-1 β , IL-18, and the cytosolic enzyme lactate dehydrogenase (LDH), an indicator of lytic cell death, into the cell culture supernatant (Figures 1A–1C, S1A, and S1B). By contrast, we detected no LDH, IL-18, or IL-1 β in the supernatants of LPS + nigericin-treated THP-1 cells deficient for caspase-1 (Figures 1A–1C, S1A, and S1B).

We then quantified the catalytic efficiency of caspase-1 on various substrates *in vitro*^{33,34} (Figures 1D and S1C–S1F). Human caspase-1 consisting of the large p20 subunit (containing the catalytic residue C285) and the small p10 subunit were co-expressed, purified, and refolded from *E. coli*. The substrates pro-IL-18 and pro-IL-1 β were expressed and purified from Sf9

insect cells, while pro-IL-37 and GSDMD were expressed and purified from *E. coli*. We found that caspase-1 cleaved pro-IL-1 β and pro-IL-18 with similar efficiency, while cleavage of pro-IL-37 was \sim 10-fold less efficient. GSDMD was cleaved by caspase-1 with the highest efficiency, at least 10-fold better than any other tested substrates.

To evaluate binding independent of catalysis, the catalytic residue C285 in the p20 subunit was mutated to alanine, and the catalytically dead C285A caspase-1 mutant was used to examine its interaction with the substrates. Caspase-1 C285A and pro-IL-18 formed a co-migrating complex in gel filtration chromatography, which eluted earlier than caspase-1 C285A or pro-IL-18 alone (Figure 1E). While caspase-1 C285A alone eluted as a monomer as judged by its similar elution position as pro-IL-18, the large shift in elution position of the complex suggested that the pro-IL-18 interaction leads to dimerization of caspase-1. Previously, analytical ultracentrifugation data showed that CARD-less C285A has a weak dimerization constant of \sim 110 μ M but can be promoted to dimerize by the pan caspase inhibitor z-VAD-fmk.¹⁹ In addition, a half amount of pro-IL-18 relative to caspase-1 resulted in the shift of almost all caspase-1 (Figure S1G). By contrast, the shift in elution position in the pro-IL-1 β complex with caspase-1 C285A was minimal, suggesting that pro-IL-1 β did not stably dimerize caspase-1 despite co-migration (Figure 1F). The measured catalytic efficiencies of caspase-1 on pro-IL-1 β and pro-IL-18 were similar (Figure 1D), which may suggest that pro-IL-1 β does dimerize caspase-1, but likely with a fast off-rate that leads to dissociation during gel filtration chromatography. These data support the relatively stable complex formation of caspase-1 with pro-IL-18 in contrast to pro-IL-1 β .

Auto-processing of caspase-1 at IDL enables its cleavage of various substrates

We further investigated whether and how the auto-processing of caspase-1 might impact its substrate recognition and cleavage activity. In addition to the p20/p10 form used above (Figures 1D–1F), a number of catalytically active and inactive caspase-1 constructs were generated to mimic the potential intermediates in caspase-1 auto-processing, including the quadruple mutant D92A/D103A/D119A/E130A at the CDL that generates p33/p10,³⁵ and the IDL mutants p22/p10 (D297A/D315A) and p20/p12 (D315A/D316A) (Figure 2A). p33/p10 cleaved pro-IL-18 and pro-IL-1 β with a catalytic efficiency comparable to the p20/p10 form; by contrast, p22/p10 showed a modest decrease in its ability to cleave pro-IL-18 or pro-IL-1 β (\sim 5-fold reduced catalytic efficiency), and p20/p12 completely lost cleavage activity (Figures 2B, 2C, and S2A–S2H). p33/p10, p20/p10, and p22/p10 cleaved the chromogenic peptide substrate WEHD-pNA at a similar rate, while peptide cleavage activity was diminished for the p20/p12 variant (Figure 2D). Thus, removal of the IDL (residues 298–316) to generate p10 appeared to be essential to achieve the substrate-cleavage activity of caspase-1 on a variety of substrates, including pro-IL-18 and pro-IL-1 β , consistent with previous reports.^{36,37} *In vitro*, the CARD did not markedly affect caspase-1's catalytic activity. However, upon inflammasome activation in cells, the CARD is essential for bringing the caspase-1 catalytic domains into proximity to promote substrate-induced dimerization and activation.

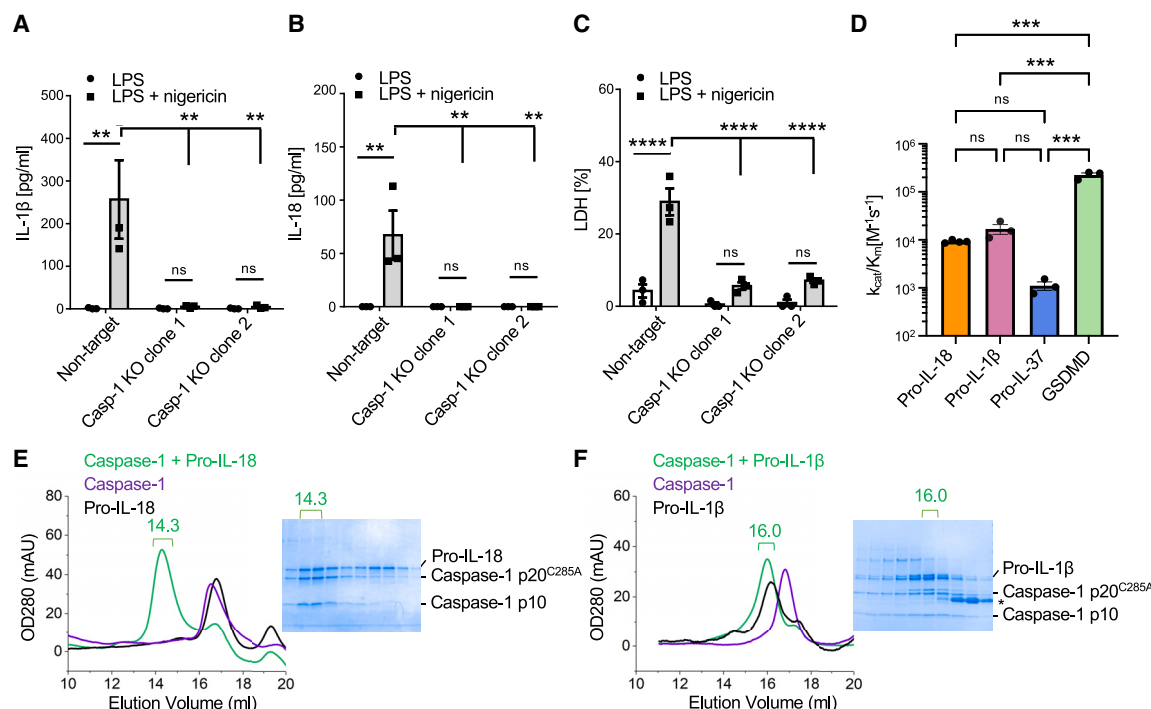


Figure 1. Biochemical characterization of caspase-1 cleavage and binding activity

(A–C) The non-target control and two clones (shown as clones 1 and 2) of *CASP1*^{−/−} THP-1 cells primed with LPS before treatment with nigericin for 2 h. IL-1β (A), IL-18 (B), and LDH (C) released into the cell culture were quantified.

(D) Quantification of caspase-1 catalytic efficiency *in vitro* (k_{cat}/K_m) on its main substrates, pro-IL-18, pro-IL-1β, pro-IL-37, and GSDMD.

(E and F) Gel filtration chromatography analysis of the binding between caspase-1 p20/p10 (C285A catalytic mutant) and pro-IL-18 (E) or pro-IL-1β (F). The elution volume of each complex is indicated. The SDS-PAGE gel containing individual fractions from the gel filtration run of the complex is shown, highlighting co-migration and complex formation. The 6 × His-SUMO tag cleaved from pro-IL-1β (F) is indicated by an asterisk.

The data shown are representative of at least three independent experiments. Bars and error bars represent the mean ± SEM of at least three independent experiments. Statistical significance was determined by one-way ANOVA with Tukey's multiple comparisons test: ns, not significant; ** $p < 0.01$; *** $p < 0.001$; **** $p < 0.0001$.

See also Figure S1.

Once CDL cleavage occurs, caspase-1 is inactivated, providing a mechanism for termination of inflammasome activation.²¹

In parallel, gel filtration chromatography using the catalytically inactive C285A forms of caspase-1 showed that pro-IL-18 co-migrated with p33/p10, similar to p20/p10 (Figures 2E and 1E). However, gel filtration chromatography only indicated a minor shift when p22/p10 was mixed with pro-IL-18 and did not detect any interaction between p20/p12 and pro-IL-18 (Figures 2F and 2G).

Cryo-EM structure determination reveals both active site and exosite interactions

To understand how caspase-1 recognizes and cleaves cytokine substrates, we determined the cryo-EM structure of the caspase-1/pro-IL-18 complex (Figure 3A). To this end, caspase-1 p20/p10 C285A was co-incubated with full-length pro-IL-18 and the resulting complex was purified by gel filtration chromatography and validated by SDS-PAGE (Figures S3A and S3B). The major peak from gel filtration was subjected to blue native PAGE to analyze its integrity and composition, which resulted in a single band near the 146 kDa marker consistent with a caspase-1/pro-IL-18 complex dimer (Figure S3C). We further stabilized the caspase-1/pro-IL-18 complex using a gradient of the

chemical amine-amine crosslinker BS3 (from 0 to 5 mM) (Figure S3C) and selected the 1 mM BS3 condition for cryo-EM sample preparation. The crosslinked complex was subjected to another step of gel filtration chromatography, the main peak of which was collected for EM analysis (Figure S3D). Negative-staining EM and cryo-EM validated the homogeneity of the sample (Figures S3E and S3F).

We first collected a cryo-EM dataset containing 4,437 raw movies, and 2D classification revealed particles with a candy-like shape (Figures 3B and S4A). 468,584 good particles were selected for initial 3D reconstruction, which showed a preferred orientation problem. Thus, an additional dataset of 3,240 raw movies was collected at a 30° stage tilt angle as suggested by calculations in an open-source software cryoEF³⁸ to diversify the orientations. 329,763 good particles were chosen from the 30° tilt dataset followed by per-particle defocus refinement. The two datasets were merged for 2D classification, and 440,340 good particles were selected for heterogeneous refinement, which revealed various conformations of the caspase-1/pro-IL-18 complex (Figure 3C). The top class consisting of 47% of total particles was subjected to homogeneous refinement with imposed 2-fold symmetry, resulting in a cryo-EM map at an overall resolution of 3.5 Å from 206,959 best particles

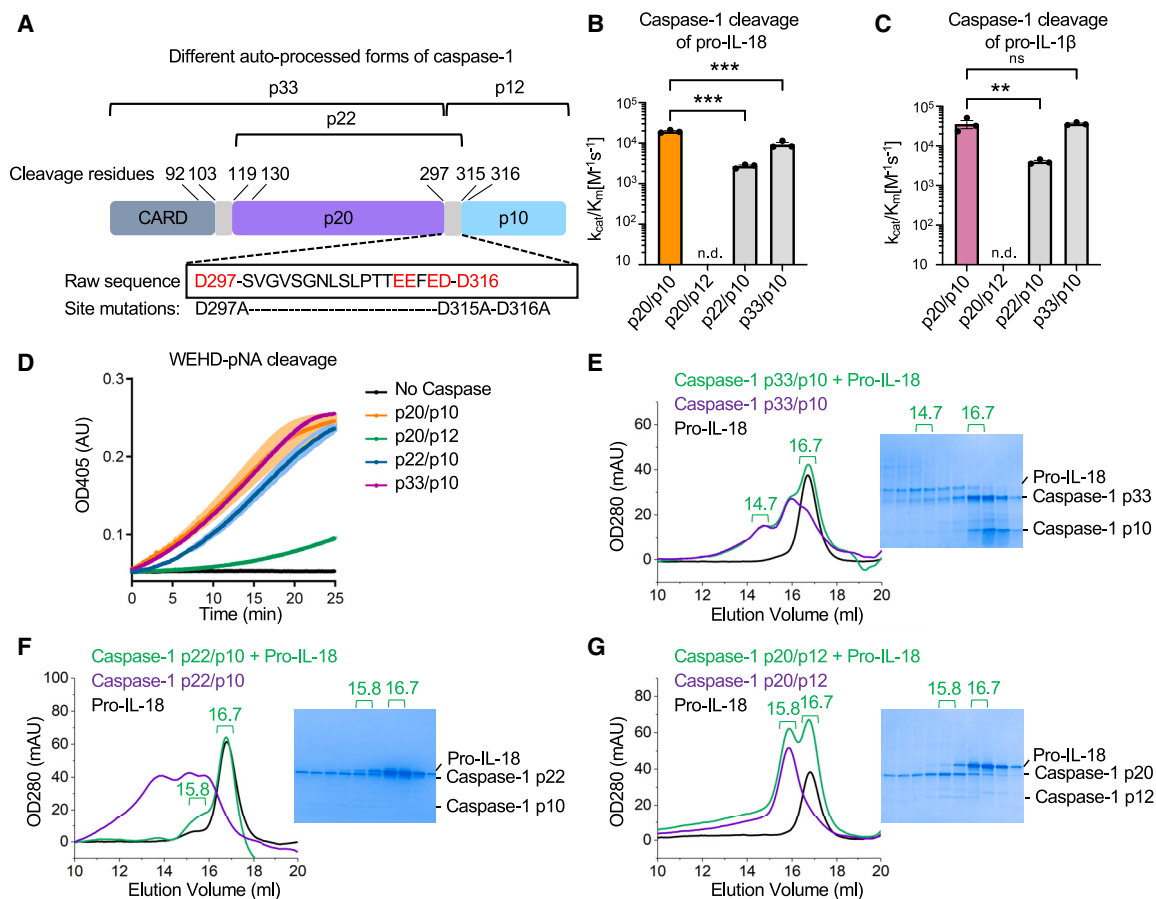


Figure 2. Complete auto-processing of caspase-1 is essential for cleavage activity

(A) The domain organization of different auto-processed forms of caspase-1 used in this study. The sequence of the linker region between p20 and p10 is shown with acidic residues in red.

(B and C) Quantification of catalytic efficiency *in vitro* of different auto-processed forms of caspase-1 on pro-IL-18 (B) or pro-IL-1β (C).

(D) Cleavage of the chromogenic peptide substrate WEHD-pNA by indicated caspase-1 forms.

(E–G) Gel filtration analysis of the binding of caspase-1 p33/p10 (E), p22/p10 (F), or p20/p12. The SDS-PAGE gel containing individual fractions from the gel filtration run of the complex indicates different degrees of complex formation. Comparison with the gel filtration analysis on the interaction between caspase-1 (p20/p10) and pro-IL-18 should refer to Figure 1E.

The data shown are representative of three independent experiments. Bars, graphs, and error bars represent the mean ± SEM of at least three independent experiments. Statistical significance was determined by one-way ANOVA with Tukey's multiple comparisons test: ***p* < 0.01; ****p* < 0.001; *****p* < 0.0001.

See also Figure S2.

(Figure S4B; Table S1). The orientational distribution of particles included in the final map is shown in Figure S4C.

In the caspase-1/pro-IL-18 complex structure, two pro-IL-18 molecules situate symmetrically at the top and bottom sides of a caspase-1 dimer when viewed down the 2-fold axis (Figures 3D and 3E). The overall map is most well defined at caspase-1 and the part of pro-IL-18 proximal to caspase-1, while the part of pro-IL-18 distal to caspase-1 exhibits more dynamics shown by 3D variability analysis (Figures 3D, 3E, and S4A; Video S1). The crystal structure of caspase-1 (PDB: 6KNO)^{35,39} fit well into the map, while the mature IL-18 structure (PDB: 3WO2)⁴⁰ exhibited large differences with the density. To explain the pro-IL-18 density, we first fitted the tetrapeptide motif of pro-IL-18 (33-LESD-36) to the caspase-1 active site and then traced the density both N- and C-terminal to the motif to complete the model building. The caspase-1 and pro-IL-18

models were then refined in real space against the map. The final model includes a caspase-1 dimer and two molecules of pro-IL-18 with the nearly complete prodomain (residues 6–36). A region of pro-IL-18 in the mature domain (residues 53–80) was not observed in the map and is likely disordered. The conformation of this class is highly similar to that of the caspase-4/pro-IL-18 structure with interactions at both the active site and the exosite (Figure 3F), but it appears that the bound pro-IL-18 in the caspase-1 complex tilts less toward the exosite than in the caspase-4 complex (Figure S4D), which may reflect its tendency to dissociate from the exosite (see below). The model of the caspase-1/pro-IL-18 complex were consistent with crosslinking mass spectrometry, with 7 and 5 pairs of crosslinks from pro-IL-18 to p10 and p20, respectively, and 2 pairs of crosslinks within the pro-IL-18 molecule (Figures S5A–S5F).

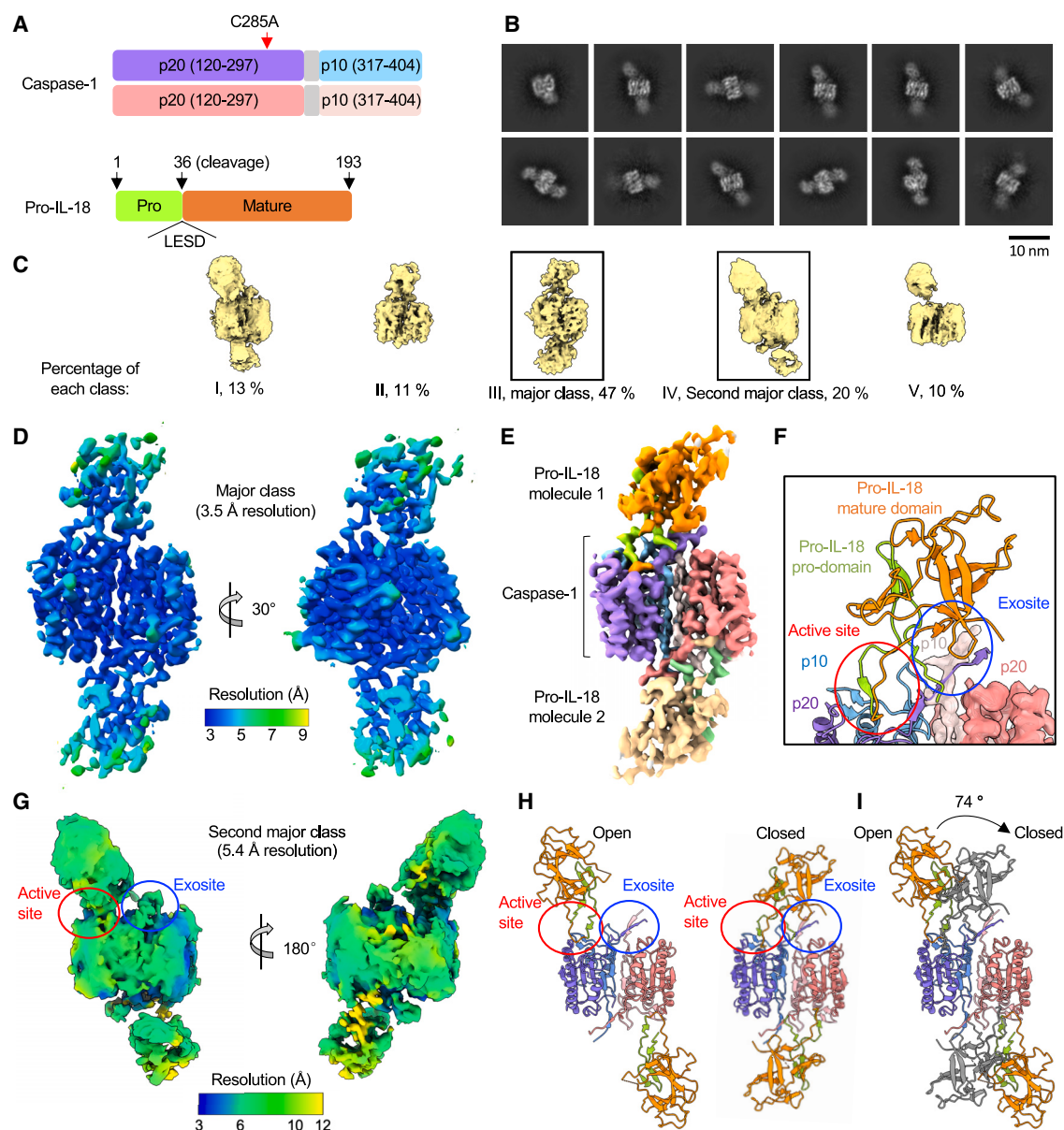


Figure 3. Cryo-EM map and model of the caspase-1/pro-IL-18 complex

(A) Domain organization of CARD-deleted caspase-1 and pro-IL-18, with p20 in light purple or coral, p10 in blue or light pink, and the removed linker between p20 and p10 in gray. The approximate location of the catalysis-inactivating C285A mutation is indicated by a red arrow. The prodomain and the mature domain of pro-IL-18 are in green and orange, respectively.

(B) Representative 2D classes of the caspase-1/pro-IL-18 complex.

(C) Homogenous refinement of the caspase-1/pro-IL-18 complex of all 3D classes without applying symmetry, showing the heterogeneity in conformations. The percentage of total particles is shown for each class.

(D and E) The cryo-EM map of the major class (III) of the caspase-1/pro-IL-18 complex (contoured at 4.0 σ), colored by local resolution (D) and by domains (E). The global resolution of the complex is 3.5 Å.

(F) The caspase-1/pro-IL-18 interaction regions, with the active site region and the exosite region blocked by red and blue rectangles, respectively. The pro-IL-18 molecule is shown as a ribbon diagram, whereas the dimer of the caspase-1 p20/p10 complex is shown as a ribbon diagram for the left monomer and a ribbon diagram superimposed with the cryo-EM map for the right monomer. Both the model and map are colored by domains.

(G) The cryo-EM map of the caspase-1/pro-IL-18 complex with one molecule of pro-IL-18 bound to caspase-1 without applied symmetry. The map is colored by local resolution (contoured at 8.0 σ). The global resolution of the complex is about 5.4 Å. Active site and exosite are highlighted in red and blue circles, respectively.

(legend continued on next page)

Caspase-1 can also engage Pro-IL-18 in an exosite-independent manner

The second major class of the caspase-1/pro-IL-18 complex (Figure 3C) revealed a distinct, open conformation. Despite the lower overall resolution of 5.4 Å, it was apparent that only active site interactions exist while the exosite site of caspase-1 does not contact pro-IL-18 (Figures 3G and 3H). In comparison with the major, closed conformation (Figure 3D), pro-IL-18 in this open conformation needs to rotate by around 74° to reach its orientation in the major (closed) conformation (Figure 3I). In addition, the different 3D classes including the minor classes I, II, and V (Figure 3C) could be interpreted as variable modes of recognition of pro-IL-18 by caspase-1, with one or two pro-IL-18 molecules binding to one caspase-1 dimer and each pro-IL-18 molecule in one of the two conformations (Figure S5G). Since caspase-1 is dimerized in all classes, we presume that both the open and closed conformations are able to induce pro-IL-18 processing. By contrast, the different 3D classes of the caspase-4/pro-IL-18 complex did not show any obvious alternative conformation.²⁶

The caspase-1/pro-IL-18 complex reveals detailed interactions at the two binding sites

We observed two binding interfaces between caspase-1 and pro-IL-18 in the complex, one at the active site, and one more distant from the active site that we named the exosite (Figures 3F, 4A, and 4B). Extensive surface areas of ~920 Å² and ~500 Å² for each binding partner are buried at the active site and exosite, respectively, as calculated by the PDBePISA server.⁴¹ In our structure, we observed extensive electrostatic interactions at or close to the tetrapeptide sequence of pro-IL-18 (33-LESD-36), including E34 and D36 of pro-IL-18 with R341 of caspase-1, E28 of pro-IL-18 with K320 of caspase-1, D29 of pro-IL-18 with R383 of caspase-1, and D36 of pro-IL-18 with R179 and H237 of caspase-1 (Figure 4A). The exosite interface has hydrophobic components in addition to electrostatic interactions (Figure 4B). A key hydrophobic exosite interaction comprises W294 of caspase-1 with I48 of pro-IL-18, and a key electrostatic exosite interaction is represented by E192 and D193 of pro-IL-18 with K296 of caspase-1 (Figure 4B). Of note, the map at the exosite is not all atomic resolution, but the involvement of these residues was validated by mutagenesis (see below). A sequence alignment among several mammalian inflammatory caspases revealed that key residues involved in the pro-IL-18 interaction are highly conserved among pro-IL-18-cleaving caspases, namely caspase-1, caspase-4, caspase-5, and canine caspase-1/4^{25,26,42} (Figure 4C). By contrast, some residues such as K320 and R383 (based on numbering in caspase-1) are not conserved in murine caspase-11, which may rationalize why caspase-11 does not process pro-IL-18 efficiently.^{42–44}

In addition to previously described effects of IDL removal on caspase-1 dimerization,³⁶ our structure may explain how the different auto-processed forms of caspase-1 influence the

cleavage activity on pro-IL-18 specifically. We hypothesize that in the p20/p12 form, the acidic residues in the IDL immediately preceding the p10 part of p12 (311-EEFEDD-316) (Figure 4D) could cause charge repulsion with the acidic surface of pro-IL-18 at the exosite, and therefore abolish the binding between p20/p12 and pro-IL-18 (Figure 4D). While p22 in the p22/p10 form will also harbor these acidic residues from the IDL, they are further away from the end of p20 and thus may exert a less repulsive effect toward the pro-IL-18 substrate in comparison with p20/p12 (Figure 4D).

Cleavage of pro-IL-18 by caspase-1 is dominated by active site interactions

Structure-guided mutagenesis was performed to validate the key residues involved in the two binding interfaces. Mutants of catalytically active and inactive forms of caspase-1 p20/p10 were generated, including substitutions to R179, R341, and R383 at, or close, to the active site and to W294 and K296 at the exosite. To assess how the caspase-1 mutations impact pro-IL-18 processing at the cellular level, we stably reconstituted caspase-1-deficient (CASP1^{−/−}) THP-1 cells with Myc-tagged caspase-1 mutants, differentiated them into macrophage-like cells by phorbol 12-myristate 13-acetate (PMA), primed them with LPS, and stimulated them with nigericin (Figures S6A and S6B). To account for potential differences in GSDMD processing by the caspase-1 mutants and thus in IL-18 release, we measured the amounts of mature IL-18 in samples combining supernatants and cell lysates. We observed that the caspase-1 active site mutants R179D, R341E, and R383E almost completely abolished IL-18 processing, with partial impairment of processing for the caspase-1 exosite mutants W294N and K296D (Figure 5A). We confirmed impaired IL-18 processing by caspase-1 mutants in supernatants and cell lysates of cells treated with LPS + nigericin by immunoblot (Figure S6C). Similar results were obtained when we performed immunoblots for IL-1β, albeit the defects for the exosite mutants (W294N and K296D) were less pronounced when compared with IL-18 (Figure S6D). The loss of pro-IL-1β from the cell lysates of cells expressing GFP or catalytically impaired caspase-1 variants following stimulation with nigericin is likely due to proteasomal degradation⁴⁵ or cleavage by caspase-3 (as indicated by the appearance of a band at around 27 kDa),⁴⁶ which becomes active as nigericin is known to induce apoptotic signaling in cells where pyroptosis is inhibited.⁴⁷

To investigate the importance of the two interaction interfaces in pro-IL-18 on caspase-1-mediated cleavage, we used IL-18-deficient (IL18^{−/−}) THP-1 macrophages reconstituted with FLAG-tagged pro-IL-18 variants carrying mutations at the active site/tetrapeptide (L33A/E34A/S35A [LES33AAA] or at the exosite E192K/D193K [ED192KK] and V47N/I48N [V47NN]) that we generated previously.²⁶ These cells were similarly stimulated with LPS + nigericin and pro-IL-18 processing was assessed by immunoblot (Figure 5B). In line with our mutagenesis studies

(H) The fitted atomic model of caspase-1 and pro-IL-18 binding via active site only (class IV, open conformation), and via both the active site and exosite (class III, closed conformation). Locations for the active site and exosite are in red and blue circles, respectively.

(I) Comparison of two modes of pro-IL-18 recognition by caspase-1. The arrow indicates the rotation needed to change from an open to a closed conformation by engaging the exosite binding.

See also Figures S3–S5 and Table S1.

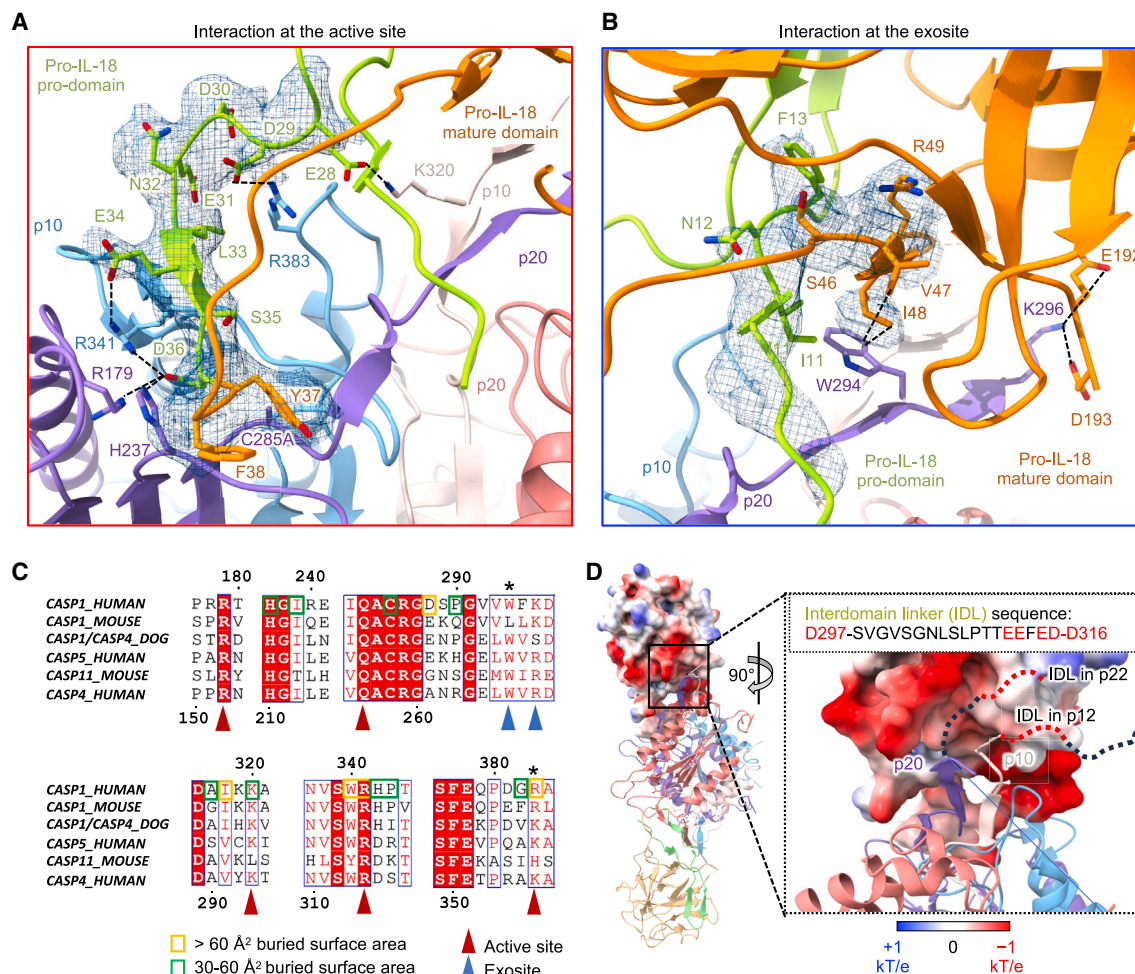


Figure 4. The interface between caspase-1 and pro-IL-18 in the complex

(A and B) Zoom-in views of the interactions at the active site region (A) and the exosite region (B). Cryo-EM densities for the prodomain of pro-IL-18 involved in the interactions are shown in blue mesh. Selective important residues are shown with side chains and labeled.

(C) Sequence alignment among caspase-1/4/5 in humans, caspase-1/11 in mice, and the hybrid of caspase-1/4 in dogs. Identical and similar amino acids are highlighted and colored in red, respectively. Sequence alignment was performed by using ClustalOmega online tool and plotted in ESPrnt 3.0. Residues with large buried surface areas in the complex are mapped at the aligned sequences, with orange rectangles for $>60 \text{ \AA}^2$ buried surface areas and green rectangles for $30\text{--}60 \text{ \AA}^2$ buried surface areas. Certain residues at the interface are indicated by red or blue arrows for the active site and the exosite, respectively. The sequence number of human caspase-1 and caspase-4 are indicated above and below the sequence alignment, respectively. * indicates the two residues with differential contributions in pro-IL-18 binding and processing by caspase-1 and caspase-4.

(D) The potential effect of the IDL linker residues in p22 and p12 for the interaction with pro-IL-18. At the left, the ribbon diagram of the complex is shown together with the electrostatic surface of pro-IL-18 in which red is for negatively charged surface, blue is for positively charged surface, and white is for neutral surface. At the right, a zoom-in view of the exosite and the IDL sequence are shown. The caspase-1 structure shown is the p20/p10 complex, and the additional IDL residues if they were included as in p22 or p12 are shown as dotted lines with red as acidic residues and black as other residues. The acidic region of the IDL included in p12 would have been closer to the negatively charged surface of pro-IL-18 and thus could affect the interaction.

See also Figure S6.

of caspase-1, cleavage of all tested pro-IL-18 mutants was reduced compared with wild-type (WT) pro-IL-18, with the active site interface mutant showing stronger effects than the exosite interface mutants.

To further evaluate the caspase-1 interfaces for their effects on cleavage of pro-IL-18, cleavage assays were performed using recombinant proteins *in vitro*. Caspase-1 mutants R341A, R383A, W294N, and K296D, as well as pro-IL-18 mutants LES33AAA at the tetrapeptide motif in the active site interface, and ED192KK and VI47NN at the exosite, were produced.

Caspase-1 mutants R179D, R341E, and R383E were excluded from the cleavage assays as we were unable to produce these proteins in *E. coli*. We observed that caspase-1 mutations at either active site or exosite impaired the catalytic efficiency, and consistent with the cellular assay, mutations at the active site were more defective those at the exosite (Figures 5A, 5C, and S6E–S6H). On the pro-IL-18 side, the active site mutation LES33AAA impaired the cleavage activity of caspase-1 much more effectively than the exosite mutants ED192KK and VI47NN (Figures 5B, 5D, and S6I–S6K). In line with the results

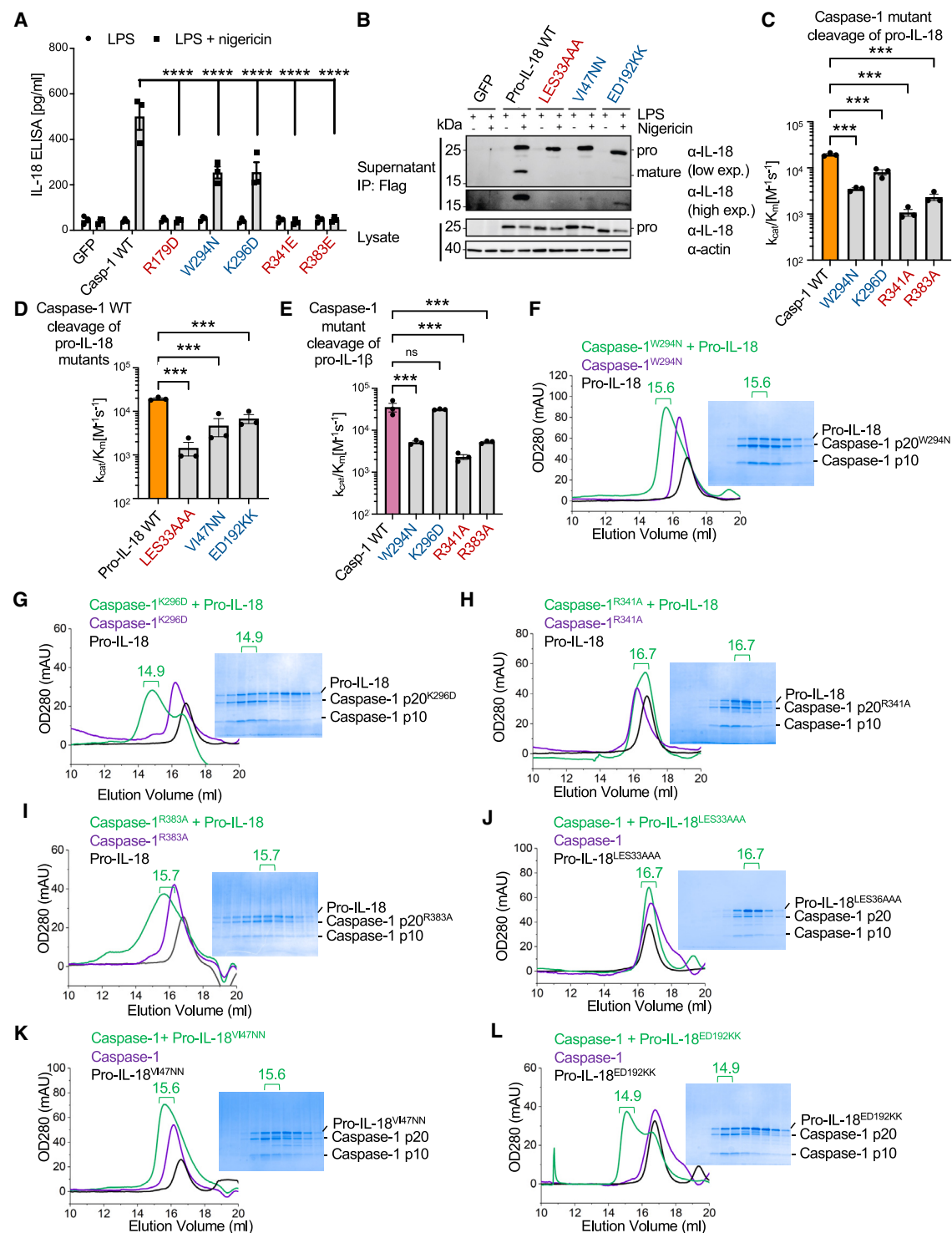


Figure 5. Mutations of key residues at the two interfaces impair the binding and cleavage of pro-IL-18 by caspase-1

(A) Mature IL-18 by ELISA in combined supernatant and cell lysate for each WT or mutant caspase-1-reconstituted *CASP1*^{-/-} THP-1 cells. White bars and filled circles: primed with LPS for 4 h; gray bars and filled rectangles: primed with LPS for 4 h followed by stimulation with nigericin for 3 h.

(B) IL-18-deficient THP-1 macrophages reconstituted with indicated pro-IL-18 variants primed with LPS for 4 h before treatment with nigericin for 2–3 h. IL-18 was immunoprecipitated from cell culture supernatants and analyzed by immunoblot.

(C and D) Quantification of *in vitro* catalytic efficiency of WT and mutant caspase-1 p20/p10 on WT pro-IL-18 (C), and of WT caspase-1 on WT and mutant pro-IL-18 (D). The pro-IL-18 WT control was the same experiment as the caspase-1 WT control.

(E) Quantification of *in vitro* catalytic efficiency of WT and mutant caspase-1 p20/p10 on pro-IL-1 β .

(legend continued on next page)

from our cell-based experiments, we obtained similar results when we used pro-IL-1 β instead of pro-IL-18 as a substrate for the indicated caspase-1 mutants (Figure 5E).

We further investigated using gel filtration chromatography if these mutations affect the binding between caspase-1 C285A and pro-IL-18. Among the caspase-1 mutants, R341A was the most defective in pro-IL-18 interaction, with W294N, K296D, and R383A exhibiting varying degrees of weakened interaction (Figures 5F–5I). Among the pro-IL-18 mutants, the LES33AAA mutant at the tetrapeptide motif had the most severe defect in its ability to interact with caspase-1 while pro-IL-18 V147NN and ED192KK were partially impaired in the interaction (Figures 5J–5L). Overall, these data show that mutations at the exosite cause less severe interaction defects than active site mutations indicating that the exosite interaction may not be as essential as the active site interaction in pro-IL-18 processing by caspase-1. This conclusion contrasts with caspase-4 for which the conserved active site residue K356 (analogous to R383 of caspase-1) was less important than the exosite residue W267 (analogous to W294 of caspase-1) for pro-IL-18 processing²⁶ (Figure 4C).

Solution NMR structure of pro-IL-18 is similar to the caspase-1 bound form but distinct from mature IL-18

Our cryo-EM structure provided a detailed model for the interaction between the pro-IL-18 substrate with caspase-1, but the absence of structural information on the apo state of pro-IL-18 limits our understanding of the pro-IL-18 maturation pathway. We therefore determined the solution structure of the apo pro-IL-18 using NMR spectroscopy. The structure calculation process and subsequent refinement resulted in a tight bundle of structures with a backbone root-mean-square deviation (RMSD) of 0.51 Å over the ordered residues (Figures 6A–6C; Table S2). As in our cryo-EM structure, the solution NMR structure of apo pro-IL-18 shows a well-packed assembly with the prodomain engaged in the β -trefoil fold. The apo form of pro-IL-18 is quite similar overall to the caspase-1 complexed state (backbone heavy atom RMSD of 1.6 Å over ordered residues); however, there are several notable differences (Figure 6D). First, the β 1' and β 2' strands are connected as one in the apo structure (Figure 6A). Second, the large disordered region (residues 53–80) that is absent in the cryo-EM structure of the complex (Figure 6D inset showing sequence) is not entirely disordered in the apo form; rather, a small β -strand, referred to as " β *," is formed by residues 55–58 (Figures 6A and 6Di). This is supported by ¹⁵N transverse relaxation rates, R_2 , which provide a measure of backbone dynamics; small ¹⁵N R_2 values are consistent with increased ps-ns timescale motion, as is often observed in the case of unstructured loop regions of proteins, while regions with larger rates are typically organized into well-defined structural elements. R_2 values for residues 55–58 are high, and rates do not show a reduction until about residue 63 (Figure 6C). The

remainder of this region (residues ~63–78), however, has lower R_2 relaxation rates than the structured regions of the protein, indicating that this region is highly flexible on the ps-ns timescale (Figure 6C). β * takes part in a mixed β -sheet with β 4 and β 5, where β * and β 4 are parallel and β 5 is antiparallel (Figure 6A). Third, the loop containing the 33-LESD-36 tetrapeptide adopts an average conformation in the apo form that is distinct from that in the complex (shown in stick representation in Figure 6Dii), where the tetrapeptide participates in critical interactions within the caspase-1 active site. However, the residues within this loop also have lower ¹⁵N R_2 relaxation rates than for the structured regions of the protein (Figure 6C), indicating a high degree of flexibility on the ps-ns timescale. This suggests that in the apo form this loop may transiently adopt a range of conformations, including poses that may be similar to that in the complex. Finally, we note that the side chain of I48, which forms a critical interaction with W294 of caspase-1 at the exosite, points into the core of pro-IL-18 in the apo form (Figure 6Diii, where the change in position of this residue is indicated by the black arrow). It is possible that binding to caspase-1 proceeds through a mechanism by which I48 transiently flips out toward the solvent in apo pro-IL-18 to allow for engagement with the enzyme, perhaps coupled to a melting of the nearby β * as in the complex. Alternatively, binding could occur in a stepwise fashion, with the first step involving interactions between the tetrapeptide and the caspase-1 active site that could then lead to perturbations in the region around I48, enabling the side chain to flip out and the exosite contacts to form in a second step.

The structure of apo pro-IL-18, similar to that of the bound form, differs substantially from the structure of mature IL-18 with RMSD of 6.5 Å over ordered backbone residues (Figure 7A). Upon alignment, the N-termini lie at opposite ends of the structures. While pro- and mature IL-18 both adopt β -trefoil folds, there are differences in the sizes and topology of the strands in the N-terminal part of these proteins (Figures 7B and 7C). The β 2' and β 3' strands of pro-IL-18 replace β 2 and β 3 of mature IL-18. The β 1' strand of pro-IL-18 does not have a counterpart in mature IL-18, whereas β 1 of pro-IL-18 becomes part of the long β 1 strand of mature IL-18 that forms an antiparallel β -sheet with β 4 and β 5 (Figure 7D). The C-terminal end of β 1 in mature IL-18 contacts β 13, somewhat similar to β 1 of pro-IL-18. Additionally, the disordered loop in pro-IL-18 (residues ~53–80), which immediately precedes β 4, is replaced by a region that contains the β 2- β 3 hairpin and an α helix (α 1) in mature IL-18 with β * in pro-IL-18 becoming part of β 2. Despite these discrepancies in the N-terminal region of the structures, β 4 through β 13 superimpose well with a backbone heavy atom RMSD of 1.9 Å over ordered residues (Figure 7A). These rearrangements of the N-terminal half of the molecule enable the 36 residue prodomain to be seamlessly incorporated into the β -trefoil fold of IL-18, producing the compact structure of pro-IL-18 presented here.

(F–L) Gel filtration analysis of the binding between mutant caspase-1 and WT pro-IL-18 (F–I) and between WT caspase-1 and mutant pro-IL-18 (J–L). The SDS-PAGE gel containing individual fractions from the gel filtration run of the complex indicates different degrees of complex formation.

The residues involved in the active site and exosite interaction are in red and blue, respectively in (A–E). The data shown are representative of three independent experiments. Bars and error bars represent the mean \pm SEM of at least three independent experiments. Statistical significance was determined by one-way ANOVA with Tukey's multiple comparisons test: ** $p < 0.01$; *** $p < 0.001$; **** $p < 0.0001$.

See also Figure S6.

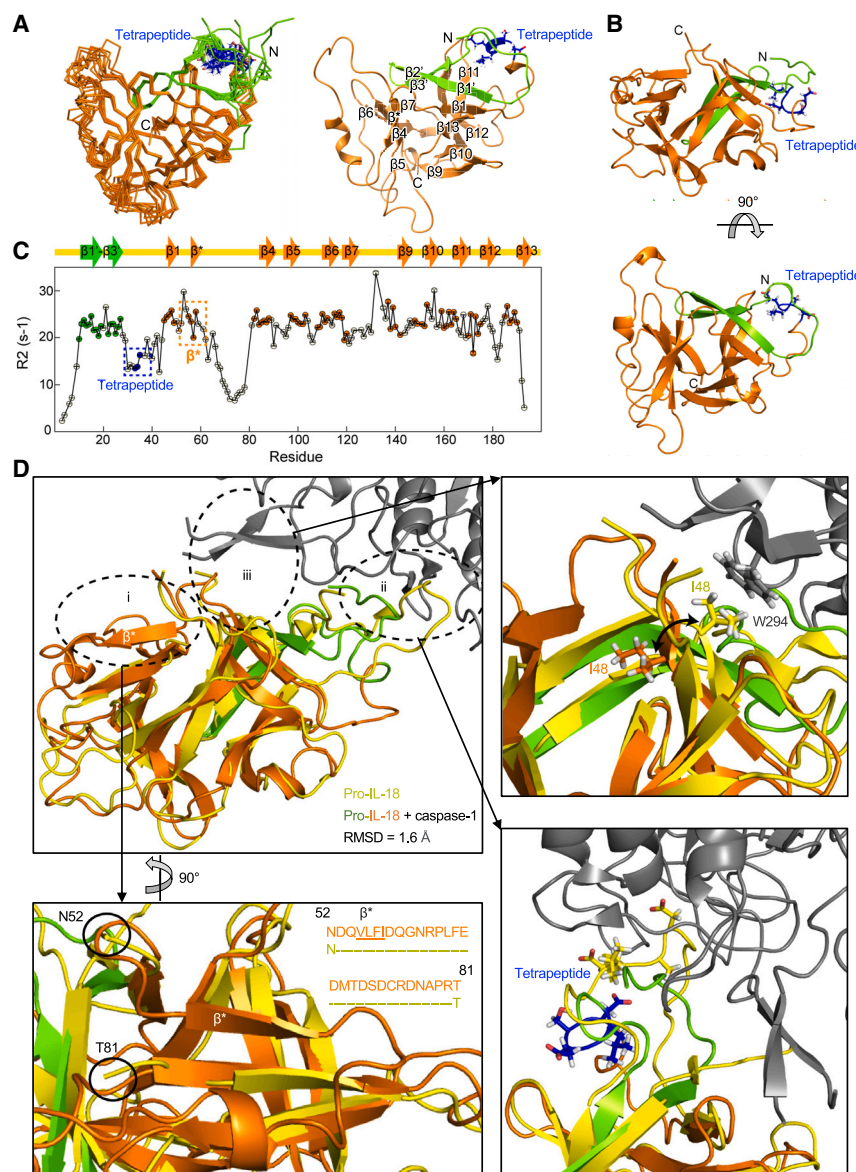


Figure 6. Solution NMR structure of apo pro-IL-18

(A) Ca trace of the NMR structure ensemble of best (lowest Rosetta scores) 10 structures resulting from CYANA structure calculation and subsequent refinement using Rosetta (see [STAR Methods](#)) (left) and a single cartoon representation of pro-IL-18 (right). Prodomain and mature domain are shown in green and orange, respectively, except that the tetrapeptide is displayed with dark blue sticks. β -strands are labeled, and “N” and “C” denote the N and C termini, respectively.

(B) The best structure of the bundle (lowest Rosetta score), shown from two different views and in domain colors except for the 33-LESD-36 tetrapeptide which is displayed with dark blue sticks.

(C) A plot of the ¹⁵N transverse relaxation rate, R_2 , of the backbone amide of each residue. As described in the text, residues with lower R_2 are more flexible on the ps-ns timescale. The data points shown in green and orange are residues within the β -strands of pro and mature domains, while the points shown in dark blue are residues of the tetrapeptide. Both the tetrapeptide and the extra β -strand, β^* , not seen in the complex, are highlighted by dashed blue and orange boxes, respectively.

(D) Overlay of cryo-EM structure of pro-IL-18 complexed with caspase-1 (yellow) with the solution NMR structure of apo pro-IL-18 (prodomain in green; mature domain in orange). While the structures are quite similar overall, with a backbone heavy atom RMSD of 1.6 Å over ordered residues (11–28, 45–60, 80–88, 97–104, 107–112, 114–120, 133–145, 147–165, 170–179, and 185–190 as determined by ¹⁵N R_2 values), several differences are highlighted. (i) Residues 53–80 are missing from the complex structure due to a lack of density. In the apo structure, this region is mostly comprised a flexible loop; however, a small β -strand involving residues 55–58 (β^*) is observed. (ii) The average orientation of the tetrapeptide-containing loop in the apo structure is distinct from that in the complex. The tetrapeptide is shown in blue sticks (apo) and yellow sticks (complex). (iii) The side chain of I48, which forms a critical exosite interaction with W294 of caspase-1 in the complex, points toward the protein core in the apo structure. The I48 side chain is shown in orange sticks (apo), and yellow sticks (complex), while the W294 side chain is shown in gray sticks. See also [Table S2](#).

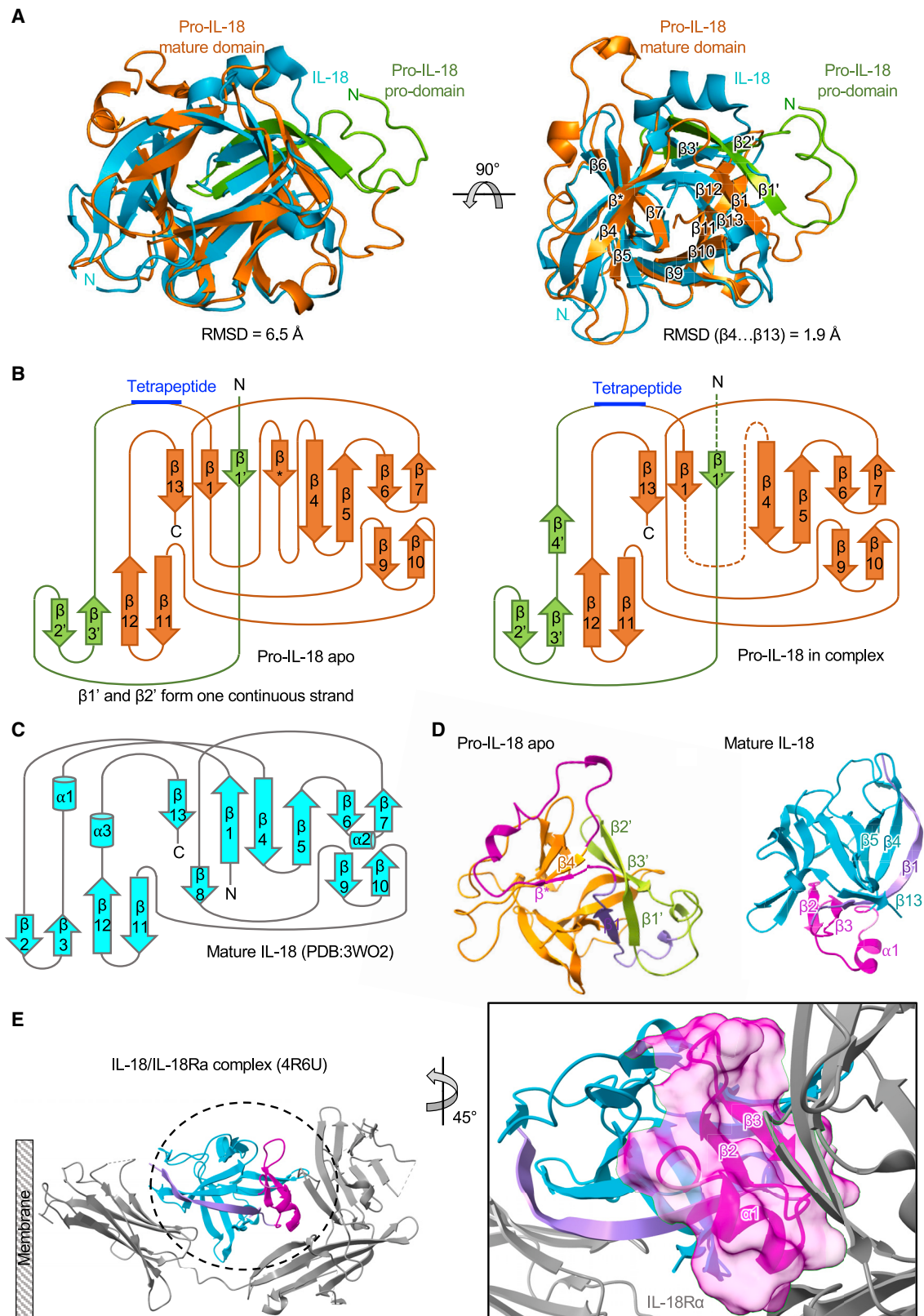
The IL-18R α -binding site is built by conformational changes upon cleavage

Mature IL-18 but not pro-IL-18 is capable of inducing inflammation in cells. To do so, mature IL-18 binds to IL-18 receptor α (IL-18R α) on target cells, and the complex in turn recruits IL-18 receptor accessory protein (IL-18Racp). The ternary IL-18/IL-18R α /IL-18Racp complex was previously characterized by x-ray crystallography.^{40,48} The IL-18R α -binding site on mature IL-18 largely involves β 2, β 3, and α 1 (Figures 7D and 7E). These structural features are absent in pro-IL-18. By trying to fit our pro-IL-18 structure into the ternary IL-18/IL-18R α /IL-18Racp complex structure, we also observed steric clashes between the tetrapeptide-containing loop in pro-IL-18 and IL-18R α (Figure S7A). In addition, the pro-IL-18 structure also clashes with IL-18 bind-

ing protein (IL-18BP) in the structure of mature IL-18 in complex with IL-18BP⁴⁹ (Figure S7B). This observation is consistent with the previous conclusion that pro-IL-18 does not bind IL-18BP.⁵⁰ Thus, caspase cleavage induces a conformational change in IL-18 that generates the IL-18R α -binding site as well as removes steric hindrance to IL-18BP and IL-18R α , the latter of which explains why uncleaved pro-IL-18 is unable to signal through the IL-18 receptor complex.

DISCUSSION

In this study, we established the mechanistic steps in the pathway for pro-IL-18 processing and the associated conformational changes that ultimately create a functional cytokine. The



(legend on next page)

significance of this finding is that it provides a structural explanation for the long-recognized problem of why cleavage of the pro-form of certain IL-1 family members is necessary to induce inflammation. Contradicting the presumption that pro-IL-18 may fold into a separate prodomain and mature domain with the caspase-cleavage site as a linker,¹⁵ we found that pro-IL-18 exhibits an overall globular fold both in the apo state and in complex with caspase-1. Pro-IL-18 binds to caspase-1 with relatively small changes in conformation, primarily on the tetrapeptide-containing segment, a long loop structure (analogous to $\beta 2$, $\beta 3$, and $\alpha 1$ in mature IL-18), and side-chain adjustment at the exosite. The conformational change in mature IL-18 upon release from the caspase-1 complex is extensive, with rearrangement of the region just after the tetrapeptide cleavage site into a long β -strand ($\beta 1$), and the neighboring long loop structure into a new β -hairpin ($\beta 2$ - $\beta 3$) and α -helix ($\alpha 1$). The new β -hairpin takes the place of the $\beta 2'$ - $\beta 3'$ hairpin in the prodomain. As such while the mature IL-18 can interact with its receptor IL-18R α , the binding site involving $\beta 2$, $\beta 3$, and $\alpha 1$ is not formed in pro-IL-18 and is additionally covered by the tetrapeptide segment. This conformational conversion elegantly preserves a similar β -trefoil fold and yet only after cleavage is the receptor-binding site created.

In addition, pro-IL-18 binding has the important effect of dimerizing caspase-1 to activate its catalytic activity. The caspase-1 catalytic domain cleaved at the IDL appears to be monomeric *in vitro* and requires substrates such as pro-IL-18 to dimerize and achieve its optimal catalytic function. This notion is consistent with deactivation of caspase-1 in cells when CDL cleavage leads to release of the cleaved catalytic domain from the inflammasome,²¹ likely due to reduced local concentration and failed substrate-induced caspase-1 dimerization.

Our caspase-1/pro-IL-18 structure resembles the recent structures of the caspase-4/pro-IL-18 complex by us and others,^{25,26} but with notable differences. In particular, we observed an alternative, open conformation in which pro-IL-18 binds caspase-1 only at the active site, not the exosite. Thus, likely because of the structural difference, a functional difference was observed in the relative contributions of the active site and the exosite in pro-IL-18 recruitment and processing by caspase-4 and caspase-1. Mutating the exosite in caspase-4 severely impairs its ability to cleave pro-IL-18 *in vitro* (almost 100-fold) and completely abolished its cleavage in cells.²⁶ By contrast, mutating the exosite in caspase-1 led to modest effects

in vitro and in cells. Hence, caspase-4 more strictly relies on the exosite for pro-IL-18 cleavage, while caspase-1 is less restricted. The dependence on exosite-mediated substrate capture may explain why caspase-4 and caspase-11 have much narrower substrate specificity compared with caspase-1.^{44,51}

Based on available structural and biochemical data, we propose a model whereby different substrates are selected and cleaved by inflammatory caspases through distinct modes of interaction. In the case of GSDMD, recognition by caspase-1, 4, and 11 is dominated by the exosite, which appears to be necessary and sufficient, while the tetrapeptide is nearly dispensable for cleavage.^{35,39} Recognition and cleavage of pro-IL-18 is more dependent on the exosite for caspase-4 than for caspase-1, but in both cases, the exosite and the active site interfaces contribute to the interaction. Whether the mode of recognition described here for pro-IL-18 extends to other IL-1 family cytokines is yet to be determined, but it may be that pro-IL-1 β is recognized by caspase-1 in a similar fashion. Consistent with this idea, exosite mutations in caspase-1 lead to detectable, but weak, defects in pro-IL-1 β processing while mutations near the active site have stronger effects.⁴² In addition, the tetrapeptide is a major determinant of efficient cleavage of pro-IL-1 β by caspase-1,²² as for pro-IL-18. The tetrapeptide found in human pro-IL-1 β (YVHD) resembles the commonly used peptide substrate YVAD, which is a high efficiency substrate for caspase-1, but a poor substrate for caspase-4 or caspase-11.^{42,44} Our data provide important insights into the mechanism of substrate recognition by caspase-1, informing on sites that should be evaluated as targets in the development of inhibitors for these critical enzymes.

Limitations of the study

Our study here comprises limitations. First, the resolution of the second major conformation of the caspase-1/pro-IL-18 complex is not sufficiently high to identify the exact amino acid residues involved to validate by mutagenesis. As a result, the relationship between the conformational heterogeneity we observe in our structural studies and the lower dependency on the exosite is only correlative. Additional structural studies on caspase-1/pro-IL-18 complexes with mutations to stabilize the second major conformation could help to address this question. Second, how caspase-1 dimerization and pro-IL-18 interaction are coupled remains unclear. Third, more studies are required to elucidate how the caspase-1/pro-IL-18 complex assembles in

Figure 7. The topology of β -trefoil fold differs in pro-IL-18 and mature IL-18

(A) The structures of apo pro-IL-18 (prodomain in green; mature domain in orange) and mature IL-18 (cyan) are overlaid. The N terminus of pro-IL-18 is indicated by the green N, while that of mature IL-18 is marked by the cyan N. While the overall alignment of the structures is quite poor (backbone heavy atom RMSD = 6.5 Å over ordered residues, see residue ranges given in Figure 6 legend), the ordered residues from $\beta 4$ through $\beta 13$ align well, with a substantially lower backbone heavy atom RMSD of 1.9 Å.

(B) Topology diagrams of pro-IL-18 apo (prodomain in green; mature domain in orange) and pro-IL-18 in complex with caspase-1. The loop that is absent in the pro-IL-18 in complex with caspase-1 is indicated by dash lines. The tetrapeptide of pro-IL-18 in apo or bound form is indicated by blue.

(C) Topology diagram of mature (cyan) IL-18 (PDB: 3WO2).

(D) The conformational difference between pro-IL-18 (left panel) and mature IL-18 (right panel), showing the structural rearrangement. For pro-IL-18, the prodomain is in green, and the mature domain is in orange except for the region immediately after the cleavage site (purple) and the following disordered loop (magenta). Mature IL-18 is in cyan except for $\beta 1$ (purple) and the $\beta 2$ - $\beta 3$ - $\alpha 1$ region (magenta). The short $\beta 1$ in pro-IL-18 rearranges into the long $\beta 1$ in mature IL-18 (purple). The β^* and the following region in pro-IL-18 rearrange into $\beta 2$ - $\beta 3$ - $\alpha 1$ in mature IL-18 (magenta).

(E) The crystal structure of the IL-18/IL-18R α complex (PDB: 4R6U) (left) and a zoom-in view (right), indicating the binding interface between mature IL-18 and IL-18R α . The $\beta 2$ - $\beta 3$ - $\alpha 1$ region in mature IL-18 participates in receptor binding.

See also Figure S7.

the context of an inflammasome, in which caspase-1 CARD forms the filamentous scaffold together with an inflammasome sensor and apoptosis-associated speck-like protein containing a caspase recruitment domain (ASC). Despite these limitations, our study provides insights into cytokine processing by caspases from a structural perspective.

STAR★METHODS

Detailed methods are provided in the online version of this paper and include the following:

- **KEY RESOURCES TABLE**
- **RESOURCE AVAILABILITY**
 - Lead contact
 - Materials availability
 - Data and code availability
- **EXPERIMENTAL MODEL AND SUBJECT DETAILS**
 - Cell lines
- **METHOD DETAILS**
 - Construct design
 - Cell-based NLRP3 inflammasome assays and immunoprecipitation of IL-1 cytokines
 - Protein expression and purification
 - Caspase-1 and pro-IL-18 complex assembly
 - Negative staining EM
 - Cryo-EM data collection
 - Cryo-EM data processing
 - Model fitting and building
 - Crosslinking mass spectrometry
 - Immunoblotting
 - *In vitro* protein cleavage assay
 - *In vitro* peptide cleavage assay
 - Gel filtration shift assay
 - Cloning, expression, purification, and sample preparation for NMR studies
 - NMR spectroscopy
 - Solution NMR structure refinement
- **QUANTIFICATION AND STATISTICAL ANALYSIS**

SUPPLEMENTAL INFORMATION

Supplemental information can be found online at <https://doi.org/10.1016/j.immuni.2024.04.015>.

ACKNOWLEDGMENTS

We thank members of the Wu lab for helpful discussions; R. Walsh, S. Sterling, M. Mayer, and S. Rawson at the Harvard Cryo-EM Center for Structural Biology for data collection at various tilting angles; and Dr. K. Song at the University of Massachusetts Cryo-EM Core for screening and preliminary dataset collection. We also thank J. Myers at the Pacific Northwest Center for Cryo-EM at Oregon Health & Science University for preliminary dataset collection, under the NIH grant U24GM129547 and accessed through EMSL (grid.436923.9), a DOE Office of Science User Facility sponsored by the Office of Biological and Environmental Research. We thank SBGrid for software and computing support. This work was supported by grants from the Canadian Institutes of Health Research FDN-503573 (to L.E.K.), and the Natural Sciences and Engineering Research Council of Canada (2015-04347) (to L.E.K.). Y.D. was supported by a postdoctoral fellowship from the Charles A. King Trust. P.D. was supported by a PhD fellowship by the Boehringer Ingelheim Fonds. J.C.K. was supported by NIH grants AI167993, AI116550, and DK34854. Z.L. was funded by National Natural Science Foundation of China (32300739) and Guangzhou Science and Technology Program City-University Joint Funding Project (Project No. 2023A03J0001).

AUTHOR CONTRIBUTIONS

H.W. conceptualized the project. Y.D., P.D., Z.L., and G.D. produced and purified recombinant proteins for biochemical and structural analyses. Y.D. generated caspase-1/pro-IL-18 samples for negative staining and cryo-EM studies. Y.D. performed cryo-EM data acquisition and processing and built and refined the model. Y.D. and P.D. performed the *in vitro* protein cleavage assay. P.D. made the stable cell lines and performed cell-based assays under J.C.K.'s supervision. J.P.B., J.M.A., and A.I.M.S. performed the solution NMR structure determination of pro-IL-18 under L.E.K.'s supervision, and J.M. performed the crosslinking mass spectrometry analysis under S.P.G.'s supervision. Y.D., J.P.B., and P.D. made most of the figures. H.W., Y.D., and P.D. wrote the manuscript with input from all authors.

DECLARATION OF INTERESTS

J.C.K. consults and holds equity in Corner Therapeutics, Larkspur Biosciences, and Neumora Therapeutics. H.W. is a co-founder and chair of the scientific advisory board of Ventus Therapeutics. None of these relationships influenced this study.

Received: October 26, 2023

Revised: February 28, 2024

Accepted: April 17, 2024

Published: May 10, 2024

REFERENCES

1. Dinarello, C.A. (2018). Overview of the IL-1 family in innate inflammation and acquired immunity. *Immunol. Rev.* 281, 8–27. <https://doi.org/10.1111/imr.12621>.
2. Afonina, I.S., Müller, C., Martin, S.J., and Beyaert, R. (2015). Proteolytic Processing of Interleukin-1 Family Cytokines: Variations on a Common Theme. *Immunity* 42, 991–1004. <https://doi.org/10.1016/j.immuni.2015.06.003>.
3. Garlanda, C., Dinarello, C.A., and Mantovani, A. (2013). The interleukin-1 family: back to the future. *Immunity* 39, 1003–1018. <https://doi.org/10.1016/j.immuni.2013.11.010>.
4. Weber, A., Wasiliew, P., and Kracht, M. (2010). Interleukin-1 (IL-1) pathway. *Sci. Signal.* 3, cm1. <https://doi.org/10.1126/scisignal.3105cm1>.
5. Chan, A.H., and Schroder, K. (2020). Inflammasome signaling and regulation of interleukin-1 family cytokines. *J. Exp. Med.* 217. <https://doi.org/10.1084/jem.20190314>.
6. Julien, O., and Wells, J.A. (2017). Caspases and their substrates. *Cell Death Differ.* 24, 1380–1389. <https://doi.org/10.1038/cdd.2017.44>.
7. Schechter, I., and Berger, A. (1967). On the size of the active site in proteases. I. Papain. *Biochem. Biophys. Res. Commun.* 27, 157–162. [https://doi.org/10.1016/s0006-291x\(67\)80055-x](https://doi.org/10.1016/s0006-291x(67)80055-x).
8. Xia, S., Zhang, Z., Magupalli, V.G., Pablo, J.L., Dong, Y., Vora, S.M., Wang, L., Fu, T.-M., Jacobson, M.P., Greka, A., et al. (2021). Gasdermin D pore structure reveals preferential release of mature interleukin-1. *Nature* 593, 607–611. <https://doi.org/10.1038/s41586-021-03478-3>.
9. Shi, J., Zhao, Y., Wang, K., Shi, X., Wang, Y., Huang, H., Zhuang, Y., Cai, T., Wang, F., and Shao, F. (2015). Cleavage of GSDMD by inflammatory caspases determines pyroptotic cell death. *Nature* 526, 660–665. <https://doi.org/10.1038/nature15514>.
10. Kayagaki, N., Stowe, I.B., Lee, B.L., O'Rourke, K., Anderson, K., Warming, S., Cuellar, T., Haley, B., Roose-Girma, M., Phung, Q.T., et al. (2015). Caspase-11 cleaves gasdermin D for non-canonical inflammasome signalling. *Nature* 526, 666–671. <https://doi.org/10.1038/nature15541>.
11. Liu, X., Zhang, Z., Ruan, J., Pan, Y., Magupalli, V.G., Wu, H., and Lieberman, J. (2016). Inflammasome-activated gasdermin D causes pyroptosis by forming membrane pores. *Nature* 535, 153–158. <https://doi.org/10.1038/nature18629>.
12. Ding, J., Wang, K., Liu, W., She, Y., Sun, Q., Shi, J., Sun, H., Wang, D.C., and Shao, F. (2016). Pore-forming activity and structural autoinhibition of

- the gasdermin family. *Nature* 535, 111–116. <https://doi.org/10.1038/nature18590>.
13. Evavold, C.L., Ruan, J., Tan, Y., Xia, S., Wu, H., and Kagan, J.C. (2018). The Pore-Forming Protein Gasdermin D Regulates Interleukin-1 Secretion from Living Macrophages. *Immunity* 48, 35–44.e6. <https://doi.org/10.1016/j.immuni.2017.11.013>.
14. Kayagaki, N., Kornfeld, O.S., Lee, B.L., Stowe, I.B., O'Rourke, K., Li, Q., Sandoval, W., Yan, D., Kang, J., Xu, M., et al. (2021). NINJ1 mediates plasma membrane rupture during lytic cell death. *Nature* 591, 131–136. <https://doi.org/10.1038/s41586-021-03218-7>.
15. Martin, S.J., Frezza, V., Davidovich, P., Najda, Z., and Clancy, D.M. (2022). IL-1 family cytokines serve as 'activity recognition receptors' for aberrant protease activity indicative of danger. *Cytokine* 157, 155935. <https://doi.org/10.1016/j.cyto.2022.155935>.
16. Cerretti, D.P., Kozlosky, C.J., Mosley, B., Nelson, N., Van Ness, K., Greenstreet, T.A., March, C.J., Kronheim, S.R., Druck, T., and Cannizzaro, L.A. (1992). Molecular cloning of the interleukin-1 beta converting enzyme. *Science* 256, 97–100. <https://doi.org/10.1126/science.1373520>.
17. Ross, C., Chan, A.H., von Pein, J.B., Maddugoda, M.P., Boucher, D., and Schroder, K. (2022). Inflammatory Caspases: Toward a Unified Model for Caspase Activation by Inflammasomes. *Annu. Rev. Immunol.* 40, 249–269. <https://doi.org/10.1146/annurev-immunol-101220-030653>.
18. Lu, A., Magupalli, V.G., Ruan, J., Yin, Q., Atianand, M.K., Vos, M.R., Schröder, G.F., Fitzgerald, K.A., Wu, H., and Egelman, E.H. (2014). Unified polymerization mechanism for the assembly of ASC-dependent inflammasomes. *Cell* 156, 1193–1206. <https://doi.org/10.1016/j.cell.2014.02.008>.
19. Datta, D., McClendon, C.L., Jacobson, M.P., and Wells, J.A. (2013). Substrate and inhibitor-induced dimerization and cooperativity in caspase-1 but not caspase-3. *J. Biol. Chem.* 288, 9971–9981. <https://doi.org/10.1074/jbc.M112.426460>.
20. Shi, J., Zhao, Y., Wang, Y., Gao, W., Ding, J., Li, P., Hu, L., and Shao, F. (2014). Inflammatory caspases are innate immune receptors for intracellular LPS. *Nature* 514, 187–192. <https://doi.org/10.1038/nature13683>.
21. Boucher, D., Monteleone, M., Coll, R.C., Chen, K.W., Ross, C.M., Teo, J.L., Gomez, G.A., Holley, C.L., Bierschenk, D., Stacey, K.J., et al. (2018). Caspase-1 self-cleavage is an intrinsic mechanism to terminate inflammasome activity. *J. Exp. Med.* 215, 827–840. <https://doi.org/10.1084/jem.20172222>.
22. Exconde, P.M., Hernandez-Chavez, C., Bray, M.B., Lopez, J.L., Srivastava, T., Egan, M.S., Zhang, J., Shin, S., Discher, B.M., and Taabazuing, C.Y. (2023). The tetrapeptide sequence of IL-1beta regulates its recruitment and activation by inflammatory caspases. Preprint at bioRxiv. <https://doi.org/10.1101/2023.02.16.528859>.
23. Chan, A.H., Burgener, S.S., Vezirgiannis, K., Wang, X., Acklam, J., Von Pein, J.B., Pizzuto, M., Labzin, L.I., Boucher, D., and Schroder, K. (2023). Caspase-4 dimerisation and D289 auto-processing elicit an interleukin-1beta-converting enzyme. *Life Sci. Alliance* 6, e202301908. <https://doi.org/10.26508/lsa.202301908>.
24. Kamens, J., Paskind, M., Hugunin, M., Talanian, R.V., Allen, H., Banach, D., Bump, N., Hackett, M., Johnston, C.G., and Li, P. (1995). Identification and characterization of ICH-2, a novel member of the interleukin-1 beta-converting enzyme family of cysteine proteases. *J. Biol. Chem.* 270, 15250–15256. <https://doi.org/10.1074/jbc.270.25.15250>.
25. Shi, X., Sun, Q., Hou, Y., Zeng, H., Cao, Y., Dong, M., Ding, J., and Shao, F. (2023). Recognition and maturation of IL-18 by caspase-4 noncanonical inflammasome. *Nature* 624, 442–450. <https://doi.org/10.1038/s41586-023-06742-w>.
26. Devant, P., Dong, Y., Mintseris, J., Ma, W., Gygi, S.P., Wu, H., and Kagan, J.C. (2023). Structural insights into cytokine cleavage by inflammatory caspase-4. *Nature* 624, 451–459. <https://doi.org/10.1038/s41586-023-06751-9>.
27. Graybill, T.L., Dolle, R.E., Helaszek, C.T., Miller, R.E., and Ator, M.A. (1994). Preparation and evaluation of peptidic aspartyl hemiacetals as reversible inhibitors of interleukin-1 beta converting enzyme (ICE). *Int. J. Pept. Protein Res.* 44, 173–182. <https://doi.org/10.1111/j.1399-3011.1994.tb00573.x>.
28. Kostura, M.J., Tocci, M.J., Limjuco, G., Chin, J., Cameron, P., Hillman, A.G., Chartrain, N.A., and Schmidt, J.A. (1989). Identification of a monocyte specific pre-interleukin 1 beta convertase activity. *Proc. Natl. Acad. Sci. USA* 86, 5227–5231. <https://doi.org/10.1073/pnas.86.14.5227>.
29. Thornberry, N.A., Bull, H.G., Calaycay, J.R., Chapman, K.T., Howard, A.D., Kostura, M.J., Miller, D.K., Molineaux, S.M., Weidner, J.R., and Aunins, J. (1992). A novel heterodimeric cysteine protease is required for interleukin-1 beta processing in monocytes. *Nature* 356, 768–774. <https://doi.org/10.1038/356768a0>.
30. Gu, Y., Kuida, K., Tsutsui, H., Ku, G., Hsiao, K., Fleming, M.A., Hayashi, N., Higashino, K., Okamura, H., Nakanishi, K., et al. (1997). Activation of interferon-gamma inducing factor mediated by interleukin-1beta converting enzyme. *Science* 275, 206–209. <https://doi.org/10.1126/science.275.5297.206>.
31. Kumar, S., Hanning, C.R., Brigham-Burke, M.R., Rieman, D.J., Lehr, R., Khandekar, S., Kirkpatrick, R.B., Scott, G.F., Lee, J.C., Lynch, F.J., et al. (2002). Interleukin-1F7B (IL-1H4/IL-1F7) is processed by caspase-1 and mature IL-1F7B binds to the IL-18 receptor but does not induce IFN-gamma production. *Cytokine* 18, 61–71. <https://doi.org/10.1006/cyto.2002.0873>.
32. Sharma, S., Kulk, N., Nold, M.F., Gräf, R., Kim, S.H., Reinhardt, D., Dinarello, C.A., and Bufler, P. (2008). The IL-1 family member 7b translocates to the nucleus and down-regulates proinflammatory cytokines. *J. Immunol.* 180, 5477–5482. <https://doi.org/10.4049/jimmunol.180.8.5477>.
33. Devant, P., and Kagan, J.C. (2022). Protocol to purify recombinant inflammatory caspases and assess their catalytic activity in vitro. *Star Protoc.* 3, 101848. <https://doi.org/10.1016/j.xpro.2022.101848>.
34. Stennicke, H.R., and Salvesen, G.S. (2000). Caspase assays. *Methods Enzymol.* 322, 91–100. [https://doi.org/10.1016/s0076-6879\(00\)22010-7](https://doi.org/10.1016/s0076-6879(00)22010-7).
35. Wang, K., Sun, Q., Zhong, X., Zeng, M., Zeng, H., Shi, X., Li, Z., Wang, Y., Zhao, Q., Shao, F., and Ding, J. (2020). Structural Mechanism for GSDMD Targeting by Autoprocessed Caspases in Pyroptosis. *Cell* 180, 941–955.e20. <https://doi.org/10.1016/j.cell.2020.02.002>.
36. Elliott, J.M., Rouge, L., Wiesmann, C., and Scheer, J.M. (2009). Crystal structure of procaspase-1 zymogen domain reveals insight into inflammatory caspase autoactivation. *J. Biol. Chem.* 284, 6546–6553. <https://doi.org/10.1074/jbc.M806121200>.
37. Ball, D.P., Taabazuing, C.Y., Griswold, A.R., Orth, E.L., Rao, S.D., Kotliar, I.B., Vostal, L.E., Johnson, D.C., and Bachovchin, D.A. (2020). Caspase-1 interdomain linker cleavage is required for pyroptosis. *Life Sci. Alliance* 3, e20200664. <https://doi.org/10.26508/lsa.20200664>.
38. Naydenova, K., and Russo, C.J. (2017). Measuring the effects of particle orientation to improve the efficiency of electron cryomicroscopy. *Nat. Commun.* 8, 629. <https://doi.org/10.1038/s41467-017-00782-3>.
39. Liu, Z., Wang, C., Yang, J., Chen, Y., Zhou, B., Abbott, D.W., and Xiao, T.S. (2020). Caspase-1 Engages Full-Length Gasdermin D through Two Distinct Interfaces That Mediate Caspase Recruitment and Substrate Cleavage. *Immunity* 53, 106–114.e5. <https://doi.org/10.1016/j.immuni.2020.06.007>.
40. Tsutsumi, N., Kimura, T., Arita, K., Ariyoshi, M., Ohnishi, H., Yamamoto, T., Zuo, X., Maenaka, K., Park, E.Y., Kondo, N., et al. (2014). The structural basis for receptor recognition of human interleukin-18. *Nat. Commun.* 5, 5340. <https://doi.org/10.1038/ncomms5340>.
41. Krissinel, E., and Henrick, K. (2007). Inference of macromolecular assemblies from crystalline state. *J. Mol. Biol.* 372, 774–797. <https://doi.org/10.1016/j.jmb.2007.05.022>.
42. Devant, P., Cao, A., and Kagan, J.C. (2021). Evolution-inspired redesign of the LPS receptor caspase-4 into an interleukin-1beta converting enzyme. *Sci. Immunol.* 6. <https://doi.org/10.1126/sciimmunol.abh3567>.

43. Bibo-Verdugo, B., Joglekar, I., Karadi Giridhar, M.N., Ramirez, M.L., Snipas, S.J., Clark, A.C., Poreba, M., and Salvesen, G.S. (2022). Resurrection of an ancient inflammatory locus reveals switch to caspase-1 specificity on a caspase-4 scaffold. *J. Biol. Chem.* 298, 101931. <https://doi.org/10.1016/j.jbc.2022.101931>.
44. Ramirez, M.L.G., Poreba, M., Snipas, S.J., Grobtorz, K., Drag, M., and Salvesen, G.S. (2018). Extensive peptide and natural protein substrate screens reveal that mouse caspase-11 has much narrower substrate specificity than caspase-1. *J. Biol. Chem.* 293, 7058–7067. <https://doi.org/10.1074/jbc.RA117.001329>.
45. Vijayaraj, S.L., Feltham, R., Rashidi, M., Frank, D., Liu, Z., Simpson, D.S., Ebert, G., Vince, A., Herold, M.J., Kueh, A., et al. (2021). The ubiquitylation of IL-1 β limits its cleavage by caspase-1 and targets it for proteasomal degradation. *Nat. Commun.* 12, 2713. <https://doi.org/10.1038/s41467-021-22979-3>.
46. Bibo-Verdugo, B., Snipas, S.J., Kolt, S., Poreba, M., and Salvesen, G.S. (2020). Extended subsite profiling of the pyroptosis effector protein gasdermin D reveals a region recognized by inflammatory caspase-11. *J. Biol. Chem.* 295, 11292–11302. <https://doi.org/10.1074/jbc.RA120.014259>.
47. Taabazuing, C.Y., Okondo, M.C., and Bachovchin, D.A. (2017). Pyroptosis and Apoptosis Pathways Engage in Bidirectional Crosstalk in Monocytes and Macrophages. *Cell Chem. Biol.* 24, 507–514.e4. <https://doi.org/10.1016/j.chembiol.2017.03.009>.
48. Wei, H., Wang, D., Qian, Y., Liu, X., Fan, S., Yin, H.S., and Wang, X. (2014). Structural basis for the specific recognition of IL-18 by its α receptor. *FEBS Lett.* 588, 3838–3843. <https://doi.org/10.1016/j.febslet.2014.09.019>.
49. Detry, S., Andries, J., Bloch, Y., Gabay, C., Clancy, D.M., and Savvides, S.N. (2022). Structural basis of human IL-18 sequestration by the decoy receptor IL-18 binding protein in inflammation and tumor immunity. *J. Biol. Chem.* 298, 101908. <https://doi.org/10.1016/j.jbc.2022.101908>.
50. Kim, S.H., Eisenstein, M., Reznikov, L., Fantuzzi, G., Novick, D., Rubinstein, M., and Dinarello, C.A. (2000). Structural requirements of six naturally occurring isoforms of the IL-18 binding protein to inhibit IL-18. *Proc. Natl. Acad. Sci. USA* 97, 1190–1195. <https://doi.org/10.1073/pnas.97.3.1190>.
51. Agard, N.J., Maltby, D., and Wells, J.A. (2010). Inflammatory stimuli regulate caspase substrate profiles. *Mol. Cell. Proteomics* 9, 880–893. <https://doi.org/10.1074/mcp.M900528-MCP200>.
52. Punjani, A., and Fleet, D.J. (2021). 3D variability analysis: Resolving continuous flexibility and discrete heterogeneity from single particle cryo-EM. *J. Struct. Biol.* 213, 107702. <https://doi.org/10.1016/j.jsb.2021.107702>.
53. Pettersen, E.F., Goddard, T.D., Huang, C.C., Couch, G.S., Greenblatt, D.M., Meng, E.C., and Ferrin, T.E. (2004). UCSF Chimera—a visualization system for exploratory research and analysis. *J. Comput. Chem.* 25, 1605–1612. <https://doi.org/10.1002/jcc.20084>.
54. Zheng, S.Q., Palovcak, E., Armache, J.P., Verba, K.A., Cheng, Y., and Agard, D.A. (2017). MotionCor2: anisotropic correction of beam-induced motion for improved cryo-electron microscopy. *Nat. Methods* 14, 331–332. <https://doi.org/10.1038/nmeth.4193>.
55. Scheres, S.H. (2012). RELION: implementation of a Bayesian approach to cryo-EM structure determination. *J. Struct. Biol.* 180, 519–30. <https://doi.org/10.1016/j.jsb.2012.09.006>.
56. Zivanov, J., Nakane, T., Forsberg, B.O., Kimanius, D., Hagen, W.J., Lindahl, E., and Scheres, S.H. (2018). New tools for automated high-resolution cryo-EM structure determination in RELION-3. *Elife* 7, e42166. <https://doi.org/10.7554/eLife.42166>.
57. Emsley, P., and Cowtan, K. (2004). Coot: model-building tools for molecular graphics. *Acta Crystallogr. D Biol. Crystallogr.* 60, 2126–2132. <https://doi.org/10.1107/S0907444904019158>.
58. Adams, P.D., Afonine, P.V., Bunkóczi, G., Chen, V.B., Davis, I.W., Echols, N., Headd, J.J., Hung, L.W., Kapral, G.J., Grosse-Kunstleve, R.W., et al. (2010). PHENIX: a comprehensive Python-based system for macromolecular structure solution. *Acta Crystallogr. D Biol. Crystallogr.* 66, 213–221. <https://doi.org/10.1107/S0907444909052925>.
59. Morin, A., Eisenbraun, B., Key, J., Sanschagrin, P.C., Timony, M.A., Ottaviano, M., and Sliz, P. (2013). Collaboration gets the most out of software. *eLife* 2, e01456. <https://doi.org/10.7554/eLife.01456>.
60. Güntert, P., Mumenthaler, C., and Wüthrich, K. (1997). Torsion angle dynamics for NMR structure calculation with the new program DYANA. *J. Mol. Biol.* 273, 283–298. <https://doi.org/10.1006/jmbi.1997.1284>.
61. Herrmann, T., Güntert, P., and Wüthrich, K. (2002). Protein NMR structure determination with automated NOE assignment using the new software CANDID and the torsion angle dynamics algorithm DYANA. *J. Mol. Biol.* 319, 209–227. [https://doi.org/10.1016/S0022-2836\(02\)00241-3](https://doi.org/10.1016/S0022-2836(02)00241-3).
62. Shen, Y., Delaglio, F., Cornilescu, G., and Bax, A. (2009). TALOS+: a hybrid method for predicting protein backbone torsion angles from NMR chemical shifts. *J. Biomol. NMR* 44, 213–223. <https://doi.org/10.1007/s10858-009-9333-z>.
63. Tejero, R., Snyder, D., Mao, B., Aramini, J.M., and Montelione, G.T. (2013). PDBStat: a universal restraint converter and restraint analysis software package for protein NMR. *J. Biomol. NMR* 56, 337–351. <https://doi.org/10.1007/s10858-013-9753-7>.
64. Bhattacharya, A., Tejero, R., and Montelione, G.T. (2007). Evaluating protein structures determined by structural genomics consortia. *Proteins* 66, 778–795. <https://doi.org/10.1002/prot.21165>.
65. Williams, C.J., Headd, J.J., Moriarty, N.W., Prisant, M.G., Videau, L.L., Deis, L.N., Verma, V., Keedy, D.A., Hintze, B.J., Chen, V.B., et al. (2018). MolProbity: More and better reference data for improved all-atom structure validation. *Protein Sci.* 27, 293–315. <https://doi.org/10.1002/pro.3330>.
66. Maciejewski, M.W., Schuyler, A.D., Gryk, M.R., Moraru, I.I., Romero, P.R., Ulrich, E.L., Eghbalnia, H.R., Livny, M., Delaglio, F., and Hoch, J.C. (2017). NMRbox: A Resource for Biomolecular NMR Computation. *Biophys. J.* 112, 1529–1534. <https://doi.org/10.1016/j.bpj.2017.03.011>.
67. Roschitzki-Voser, H., Schroeder, T., Lenherr, E.D., Frölich, F., Schweizer, A., Donepudi, M., Ganesan, R., Mittl, P.R.E., Baici, A., and Grütter, M.G. (2012). Human caspases in vitro: expression, purification and kinetic characterization. *Protein Expr. Purif.* 84, 236–246. <https://doi.org/10.1016/j.pep.2012.05.009>.
68. Punjani, A., Rubinstein, J.L., Fleet, D.J., and Brubaker, M.A. (2017). cryoSPARC: algorithms for rapid unsupervised cryo-EM structure determination. *Nat. Methods* 14, 290–296. <https://doi.org/10.1038/nmeth.4169>.
69. Klaholz, B.P. (2019). Deriving and refining atomic models in crystallography and cryo-EM: the latest Phenix tools to facilitate structure analysis. *Acta Crystallogr. D Struct. Biol.* 75, 878–881. <https://doi.org/10.1107/S2059798319013391>.
70. Goddard, T.D., Huang, C.C., Meng, E.C., Pettersen, E.F., Couch, G.S., Morris, J.H., and Ferrin, T.E. (2018). UCSF ChimeraX: Meeting modern challenges in visualization and analysis. *Protein Sci.* 27, 14–25. <https://doi.org/10.1002/pro.3235>.
71. Mintseris, J., and Gygi, S.P. (2020). High-density chemical cross-linking for modeling protein interactions. *Proc. Natl. Acad. Sci. USA* 117, 93–102. <https://doi.org/10.1073/pnas.1902931116>.
72. Boucher, D., Duclos, C., and Denault, J.B. (2014). General in vitro caspase assay procedures. *Methods Mol. Biol.* 1133, 3–39. https://doi.org/10.1007/978-1-4939-0357-3_1.
73. Covington, A.K., Paabo, M., Robinson, R.A., and Bates, R.G. (1968). Use of the glass electrode in deuterium oxide and the relation between the standardized pD (paD) scale and the operational pH in heavy water. *Anal. Chem.* 40, 700–706. <https://doi.org/10.1021/ac60260a013>.
74. Delaglio, F., Grzesiek, S., Vuister, G.W., Zhu, G., Pfeifer, J., and Bax, A. (1995). NMRPipe: a multidimensional spectral processing system based on UNIX pipes. *J. Biomol. NMR* 6, 277–293. <https://doi.org/10.1007/BF00197809>.

75. Lee, W., Tonelli, M., and Markley, J.L. (2015). NMRFAM-SPARKY: enhanced software for biomolecular NMR spectroscopy. *Bioinformatics* 31, 1325–1327. <https://doi.org/10.1093/bioinformatics/btu830>.
76. Lee, W., Bahrami, A., Dashti, H.T., Eghbalnia, H.R., Tonelli, M., Westler, W.M., and Markley, J.L. (2019). I-PINE web server: an integrative probabilistic NMR assignment system for proteins. *J. Biomol. NMR* 73, 213–222. <https://doi.org/10.1007/s10858-019-00255-3>.
77. Kay, L., Keifer, P., and Saarinen, T. (1992). Pure absorption gradient enhanced heteronuclear single quantum correlation spectroscopy with improved sensitivity. *J. Am. Chem. Soc.* 114, 10663–10665. <https://doi.org/10.1021/ja00052a088>.
78. Sattler, M., Schleucher, J., and Griesinger, C. (1999). Heteronuclear multi-dimensional NMR experiments for the structure determination of proteins in solution employing pulsed field gradients. *Progress in Nuclear Magnetic Resonance Spectroscopy* 34, 93–158. [https://doi.org/10.1016/S0079-6565\(98\)00025-9](https://doi.org/10.1016/S0079-6565(98)00025-9).
79. Panchal, S.C., Bhavesh, N.S., and Hosur, R.V. (2001). Improved 3D triple resonance experiments, HNN and HN(C)N, for HN and 15N sequential correlations in (13C, 15N) labeled proteins: application to unfolded proteins. *J. Biomol. NMR* 20, 135–147. <https://doi.org/10.1023/a:1011239023422>.
80. Grzesiek, S., and Bax, A. (1993). Amino acid type determination in the sequential assignment procedure of uniformly 13C/15N-enriched proteins. *J. Biomol. NMR* 3, 185–204. <https://doi.org/10.1007/BF00178261>.
81. Montelione, G.T., Lyons, B.A., Emerson, S.D., and Tashiro, M. (1992). An efficient triple resonance experiment using carbon-13 isotropic mixing for determining sequence-specific resonance assignments of isotopically-enriched proteins. *J. Am. Chem. Soc.* 114, 10974–10975. <https://doi.org/10.1021/ja00053a051>.
82. Neri, D., Szyperski, T., Otting, G., Senn, H., and Wüthrich, K. (1989). Stereospecific nuclear magnetic resonance assignments of the methyl groups of valine and leucine in the DNA-binding domain of the 434 repressor by biosynthetically directed fractional 13C labeling. *Biochemistry* 28, 7510–7516. <https://doi.org/10.1021/bi00445a003>.
83. Santoro, J., and King, G.C. (1992). A constant-time 2D overbroadenhausen experiment for inverse correlation of isotopically enriched species. *J. Magn. Reson.* 1969 97, 202–207. [https://doi.org/10.1016/0022-2364\(92\)90250-B](https://doi.org/10.1016/0022-2364(92)90250-B).
84. Vuister, G.W., and Bax, A. (1992). Resolution enhancement and spectral editing of uniformly 13C-enriched proteins by homonuclear broadband 13C decoupling. *J. Magn. Reson.* 1969 98, 428–435. [https://doi.org/10.1016/0022-2364\(92\)90144-V](https://doi.org/10.1016/0022-2364(92)90144-V).
85. Yamazaki, T., Forman-Kay, J.D., and Kay, L.E. (1993). Two-dimensional NMR experiments for correlating carbon-13. beta. and proton. delta./epsilon. chemical shifts of aromatic residues in 13C-labeled proteins via scalar couplings. *J. Am. Chem. Soc.* 115, 11054–11055. <https://doi.org/10.1021/ja00076a099>.
86. Bax, A., Max, D., and Zax, D. (1992). Measurement of long-range 13C-13C J couplings in a 20-kDa protein-peptide complex. *J. Am. Chem. Soc.* 114, 6923–6925. <https://doi.org/10.1021/ja00043a052>.
87. Grzesiek, S., Vuister, G.W., and Bax, A. (1993). A simple and sensitive experiment for measurement of JCC couplings between backbone carbonyl and methyl carbons in isotopically enriched proteins. *J. Biomol. NMR* 3, 487–493. <https://doi.org/10.1007/BF00176014>.
88. Vuister, G.W., Wang, A.C., and Bax, A. (1993). Measurement of three-bond nitrogen-carbon J couplings in proteins uniformly enriched in nitrogen-15 and carbon-13. *J. Am. Chem. Soc.* 115, 5334–5335. <https://doi.org/10.1021/ja00065a071>.
89. Hu, J.-S., Grzesiek, S., and Bax, A. (1997). Two-dimensional NMR methods for determining α_1 angles of aromatic residues in proteins from three-bond J coupling. *J. Am. Chem. Soc.* 119, 1803–1804. <https://doi.org/10.1021/ja963625z>.
90. Marion, D., Kay, L.E., Sparks, S.W., Torchia, D.A., and Bax, A. (1989). Three-dimensional heteronuclear NMR of nitrogen-15 labeled proteins. *J. Am. Chem. Soc.* 111, 1515–1517. <https://doi.org/10.1021/ja00186a066>.
91. Ikura, M., Kay, L.E., Tschudin, R., and Bax, A. (1990). Three-dimensional NOESY-HMQC spectroscopy of a 13C-labeled protein. *J. Magn. Reson.* 1969 86, 204–209. [https://doi.org/10.1016/0022-2364\(90\)90227-Z](https://doi.org/10.1016/0022-2364(90)90227-Z).
92. Hyberts, S.G., Takeuchi, K., and Wagner, G. (2010). Poisson-gap sampling and forward maximum entropy reconstruction for enhancing the resolution and sensitivity of protein NMR data. *J. Am. Chem. Soc.* 132, 2145–2147. <https://doi.org/10.1021/ja908004w>.
93. Ying, J., Delaglio, F., Torchia, D.A., and Bax, A. (2017). Sparse multidimensional iterative lineshape-enhanced (SMILE) reconstruction of both non-uniformly sampled and conventional NMR data. *J. Biomol. NMR* 68, 101–118. <https://doi.org/10.1007/s10858-016-0072-7>.
94. Cavanagh, J., Fairbrother, W.J., Palmer, A.G., Rance, M., and Skelton, N.J. (2007). *Protein NMR Spectroscopy*, Second Edition (Academic Press).
95. Farrow, N.A., Muhandiram, R., Singer, A.U., Pascal, S.M., Kay, C.M., Gish, G., Shoelson, S.E., Pawson, T., Forman-Kay, J.D., and Kay, L.E. (1994). Backbone dynamics of a free and phosphopeptide-complexed Src homology 2 domain studied by 15N NMR relaxation. *Biochemistry* 33, 5984–6003. <https://doi.org/10.1021/bi00185a040>.
96. Tyka, M.D., Keedy, D.A., André, I., Dimaio, F., Song, Y., Richardson, D.C., Richardson, J.S., and Baker, D. (2011). Alternate states of proteins revealed by detailed energy landscape mapping. *J. Mol. Biol.* 405, 607–618. <https://doi.org/10.1016/j.jmb.2010.11.008>.
97. Nivón, L.G., Moretti, R., and Baker, D. (2013). A Pareto-optimal refinement method for protein design scaffolds. *PLoS One* 8, e59004. <https://doi.org/10.1371/journal.pone.0059004>.

STAR★METHODS

KEY RESOURCES TABLE

REAGENT or RESOURCE	SOURCE	IDENTIFIER
Antibodies		
Anti-human IL-18	MBL International	Cat# PM014; RRID:AB_592017
Anti-human caspase-1	Cell Signaling Technology	Cat# 3866; RRID:AB_2069051
Anti-cMyc	Cell Signaling Technology	Cat# 18583; RRID:AB_2895543
Anti-human IL-1 β	R and D Systems	Cat# AF-401-NA; RRID:AB_416684
Anti-human IL-1 β	Genetex	Cat# GTX130021; RRID:AB_2886157
Anti-human GSDMD	Cell signaling	Cat# 93709S; RRID:AB_2800210
Anti- β -actin	Sigma Aldrich	Cat# A1978; RRID:AB_476692
Anti-Myc-tag	Cell Signaling Technology	Cat# 2278; RRID:AB_490778,
Biotinylated anti-IL-1 β	R and D Systems	Cat# BAF201; RRID:AB_356214
Goat Anti-Rabbit IgG, HRP conjugated	BD Biosciences	Cat# 554021; RRID:AB_395213
Rabbit Anti-Goat IgG, HRP conjugated	R and D Systems	Cat# HAF017; RRID:AB_562588
Peroxidase AffiniPure Goat Anti-Mouse IgG (H+L)	Jackson ImmunoResearch	Cat# 115-035-003; RRID:AB_10015289
Peroxidase AffiniPure Goat Anti-Rabbit IgG (H+L)	Jackson ImmunoResearch	Cat# 111-035-003; RRID:AB_2313567
Bacterial and virus strains		
<i>E. coli</i> BL21(DE3)	New England Biolabs	Cat# C2527
<i>E. coli</i> DH5- α	New England Biolabs	Cat# C2987
DH10Bac	ThermoFisher (GIBCO)	Cat# 10361-012
Chemicals, peptides, and recombinant proteins		
Protease Inhibitor Cocktail	Sigma-Aldrich	Cat# P8849
Trizma® base	Sigma-Aldrich	Cat# T1503
HEPES	Sigma-Aldrich	Cat# H3375
Sodium Chloride	Sigma-Aldrich	Cat# S5886
Glycerol	Sigma-Aldrich	Cat# G6279
Sucrose	Sigma-Aldrich	Cat# S0389
Phosphate buffered saline	Sigma-Aldrich	Cat#P3813
Triton X-100	Sigma-Aldrich	Cat#T8787
Tween 20	Sigma-Aldrich	Cat# P9416
Sodium acetate	Sigma-Aldrich	Cat# S2889
Guanidine hydrochloride	Sigma-Aldrich	Cat# 50950
Ethylenediaminetetraacetic acid disodium salt (EDTA disodium salt)	Sigma-Aldrich	Cat# E5134
Sodium malonate dibasic	Sigma-Aldrich	Cat# 63409
NDSB-201	Sigma-Aldrich	Cat# sc-202237A
PIPES	Sigma-Aldrich	Cat# P6757
Chaps hydrate	Sigma-Aldrich	Cat# C5070
PMA	Sigma-Aldrich	Cat# P1585
Hydroxylamine solution	Sigma-Aldrich	Cat# 438227
Imidazole, reagentplus®, 99%	Sigma-Aldrich	Cat# I202
D-(+)-Glucose, $\geq 99.5\%$ (GC)	Sigma-Aldrich	Cat# G8270
15NH ₄ Cl	Sigma-Aldrich	Cat # 299251-50G

(Continued on next page)

Continued

REAGENT or RESOURCE	SOURCE	IDENTIFIER
Isopropyl-b-D-thiogalactopyranoside (IPTG)	Goldbio	Cat# I2481C10
Protogel acrylamide solution	National Diagnostics	Cat# EC-809
Protogel stacking buffer	National Diagnostics	Cat# EC-893
Protogel resolving buffer	National Diagnostics	Cat# EC-892
TEMED	Sigma-Aldrich	Cat# T9281-100ML
Ammonium persulfate	Thermo Fisher Scientific	Cat# 17874
Ac-WEHD-pNA	Enzo	Cat# ALX-260-082-M005
zVAD(OH)-fmk	Cayman Chemical	Cat# 14467
Dithiothreitol	Goldbio	Cat# DTT100
Cellfectin II Reagent	Invitrogen	Cat# 10362-100
LPS	Invivogen	Cat#tlrl-b5lps
LPS E. coli Serotype O55:B5	Enzo Life Science	Cat# ALX-581-013
TEV protease	Hao Wu Lab	N/A
SUMO protease	Hao Wu Lab	N/A
Uranyl formate hydrate	Electron Microscopy Sciences	Cat# 22450
DPBS	ThermoFisher	Cat# 14190250
Native PAGE running buffer	ThermoFisher	Cat#BN2001
Cathode buffer additive	ThermoFisher	Cat#BN2002
HyClone™ SFX-Insect™ Media	Fisher Scientific	Cat# SH30278LS
RPMI 1640 Medium	Thermo Fisher Scientific	Cat# 11-875-093
Bs3 (bis(sulfosuccinimidyl)suberate)	Fisher Scientific	Cat# A39266
Ni-NTA Agarose	QIAGEN 30230	Cat# 30230
SDS-PAGE Sample Loading Buffer [6X]	G Biosciences	Cat# 786-701
TCEP hydrochloride	Hampton Research	Cat# HR2-801
Kid Enzyme Mix	New England Biolabs	Cat# M0554S
Q5 High-Fidelity 2X Master Mix	New England Biolabs	Cat# M0492L
Dulbecco's MEM, high glucose, L-glut,pyruvate	ThermoFisher Scientific	Cat# 11995-073
L-glutamine	ThermoFisher Scientific	Cat# 25030081
Lipofectamine 2000	Invitrogen	Cat# 11668019
Nigericin	Invivogen	Cat# tlrl-nig
Neutravidine agarose	ThermoFisher Scientific	Cat# 29200
Anti-FLAG M2 Affinity gel	MilliporeSigma	Cat# A2220
OptiMEM reduced serum media	ThermoFisher Scientific	Cat# 31985062
Pen/Strep	ThermoFisher Scientific	Cat# 15-140-122
Phusion HF Polymerase	ThermoFisher Scientific	Cat# F-530L
Polybrene	MerckMillipore	Cat# TR-1003-G
Sodium Pyruvate	ThermoFisher Scientific	Cat# 11360070
¹³ C-glucose	Cambridge isotope Laboratories	Cat # CLM-1396-50
D2O	Cambridge isotope Laboratories	Cat # DLM-4-1000
Critical commercial assays		
Human IL-18 ELISA kit	R and D Systems	Cat# DY318-05
Human IL-1β ELISA kit	R and D Systems	Cat# DY201-05
Q5® Site-Directed Mutagenesis Kit	New England Biolabs	Cat# E0552S
Gibson Assembly Cloning Kit	New England Biolabs	Cat# E5510S
CyQUANT™ LDH Cytotoxicity Assay	Thermo Fisher Scientific	Cat# C20300

(Continued on next page)

Continued

REAGENT or RESOURCE	SOURCE	IDENTIFIER
Deposited data		
Cryo-EM map of caspase-1/pro-IL-18 complex	This paper	EMD-40781
Coordinate of caspase-1/pro-IL-18 complex	This paper	PDB: 8SV1
NMR structure of pro-IL-18 apo	This paper	PDB: 8URV BMRB: 31122
Experimental models: Cell lines		
THP1 cells + Non-target sgRNA	Devant et. al. ²⁶	N/A
THP1 cells <i>CASP1</i> ^{-/-}	Devant et. al. ²⁶	N/A
THP1 cells <i>CASP1</i> ^{-/-} + GFP only	This paper	N/A
THP1 cells <i>CASP1</i> ^{-/-} + Caspase-1 WT	This paper	N/A
THP1 cells <i>CASP1</i> ^{-/-} + Caspase-1 R179D	This paper	N/A
THP1 cells <i>CASP1</i> ^{-/-} + Caspase-1 W294N	This paper	N/A
THP1 cells <i>CASP1</i> ^{-/-} + Caspase-1 K296D	This paper	N/A
THP1 cells <i>CASP1</i> ^{-/-} + Caspase-1 R341E	This paper	N/A
THP1 cells <i>CASP1</i> ^{-/-} + Caspase-1 R383E	This paper	N/A
THP1 cell <i>IL18</i> ^{-/-} + GFP	Devant et. al. ²⁶	N/A
THP1 cell <i>IL18</i> ^{-/-} + pro-IL-18 WT	Devant et. al. ²⁶	N/A
THP1 cell <i>IL18</i> ^{-/-} + pro-IL-18 LES33AAA	Devant et. al. ²⁶	N/A
THP1 cell <i>IL18</i> ^{-/-} + pro-IL-18 VI47NN	Devant et. al. ²⁶	N/A
THP1 cell <i>IL18</i> ^{-/-} + pro-IL-18 ED192KK	Devant et. al. ²⁶	N/A
SF9 cells	ThermoFisher (GIBCO)	Cat# B82501
Recombinant DNA		
pET21a caspase-1 p20 (120-297)	Dr. Tsan Sam Xiao	N/A
pET21a caspase-1 p10 (317-404)	Dr. Tsan Sam Xiao	N/A
pSUMO Caspase-1 p20 (120-297) C285A	Dr. Feng Shao	N/A
pET21b Casp1-His	Addgene	Plasmid# 11809
pET21a caspase-1 p20 (120-297) W294N	This study	N/A
pET21a caspase-1 p20 (120-297) K296D	This study	N/A
pET21a caspase-1 p10 (317-404) R341A	This study	N/A
pET21a caspase-1 p10 (317-404) R383A	This study	N/A
pET21a caspase-1 p33 (1-297) D92A/ D103A/D119A/E130A	This study	N/A
pET21a caspase-1 p22 (120-316) D297A/D315A	This study	N/A
pET21a caspase-1 p12 (298-404) D315A/D316A	This study	N/A
pMSCV-IRES-EGFP caspase-1	Devant et. al. ²⁶	Addgene #183359
pMSCV-IRES-EGFP caspase-1 R179D	This study	N/A
pMSCV-IRES-EGFP caspase-1 W294N	This study	N/A
pMSCV-IRES-EGFP caspase-1 K296D	This study	N/A
pMSCV-IRES-EGFP caspase-1 R341E	This study	N/A
pMSCV-IRES-EGFP caspase-1 R383E	This study	N/A
pSUMO Caspase-1 p20 (120-297) C285A/W294N	This study	N/A
pSUMO Caspase-1 p20 (120-297) C285A/K296D	This study	N/A
pSUMO Caspase-1 p10 (317-404) C285A/R341A	This study	N/A

(Continued on next page)

Continued

REAGENT or RESOURCE	SOURCE	IDENTIFIER
pSUMO Caspase-1 p10 (317-404) C285A/ R383A	This study	N/A
pSUMO Caspase-1 p33 (1-297) D92A/ D103A/D119A/E130A/C285A	This study	N/A
pSUMO caspase-1 p22 (120-316) C285A/ D297A/D315A	This study	N/A
pSUMO caspase-1 p12 (298-404) C285A/ D315A/D316A	This study	N/A
pET SUMO vector	ThermoFisher Scientific	Cat# K30001
pET SUMO human pro-IL-18	This study	N/A
pET28a human pro-IL-18	Devant et. al. ⁴²	Addgene # 183390
pET28a human pro-IL-18 LES33AAA	Devant et. al. ²⁶	Addgene # 214326
pET28a human pro-IL-18 VI47NN	Devant et. al. ²⁶	Addgene # 214323
pET28a human pro-IL-18 ED192KK	Devant et. al. ²⁶	Addgene # 214322
pFastBac human pro-IL-18	Devant et. al. ²⁶	Addgene #214317
pFastBac human pro-IL-1 β	This study	N/A
Software and algorithms		
SerialEM	Mastronarde	http://bio3d.colorado.edu/SerialEM
CryoSPARC	Punjani et al. ⁵²	https://cryosparc.com/download/
UCSF ChimeraX 1.6	Pettersen et al. ⁵³	https://www.rbvi.ucsf.edu/chimerax/SBGrid Morin et al. 70 RRID: SCR_003511
Fiji ImageJ	NIH	https://fiji.sc/
Origin 8.0	OriginLab Corporation, Northampton, MA, USA	https://www.originlab.com
MotionCor2	Zheng et al. ⁵⁴	http://msg.ucsf.edu/em/software/motioncor2.html
Relion3.0.8	Scheres ⁵⁵ ; Zivanov et al. ⁵⁶	https://relion.readthedocs.io/en
UCSF Chimera	Pettersen et al. ⁵³	https://www.cgl.ucsf.edu/chimera/
Cryo-EF	Naydenova and Russo ³⁸	https://www.mrc-lmb.cam.ac.uk/crusso/cryoEF/
3D variability analysis (3DVA)	Punjani and Fleet ⁵²	https://doi.org/10.1016/j.jsb.2021.107702
PyMol	Schrodinger, LLC., 2015	https://pymol.org/2/
COOT	Emsley et al. ⁵⁷	https://www2.mrc-lmb.cam.ac.uk/personal/pemsley/coot
PHENIX	Adams et al. ⁵⁸	https://www.phenix-online.org
Prism 9	GraphPad	https://www.graphpad.com/
Illustrator CC 2019	Adobe	https://www.adobe.com/products/illustrator.html
SparkControl v.3.2	Tecan	N/A
PISA	EMBL-EBI	https://www.ebi.ac.uk/pdbe/pisa/
SBGrid	Morin et al. ⁵⁹	RRID: SCR_003511
CYANA (3.98.15)	Guntert et al. Herrmann et al. ^{60,61}	https://cyana.org
TALOS+	Shen et al. ⁶²	http://spin.niddk.nih.gov/bax/software/TALOS+/index.html
PdbStat	Tejero et al. ⁶³	https://nmrbox.nmrhub.org/software/pdbstat
PSVS 2.0	Bhattacharya et al. ⁶⁴	https://montelionelab.chem.rpi.edu/PSVS/PSVS/
MolProbity	Williams et al. ⁶⁵	http://molprobity.biochem.duke.edu
NMRbox	Maciejewski et al. ⁶⁶	https://nmrbox.nmrhub.org
Biorender	Biorender	https://help.biorender.com/en

(Continued on next page)

Continued

REAGENT or RESOURCE	SOURCE	IDENTIFIER
Other		
Superdex 200 increase 10/300 GL column	Cytiva	Cat# 28990944
HiTrap SP HP, 5 ml	Cytiva	Cat# 17-1152-01
Amicon ultra 10 kDa cutoff	Millipore Sigma	Cat# UFC801096
Amicon Ultra 30 kDa cutoff	Millipore Sigma	Cat# UFC903024
4–15% Mini-PROTEAN TGX Precast Protein Gels	BIO-RAD	Cat# 4561086
4–20% Mini-PROTEAN TGX Precast Protein Gels	BIO-RAD	Cat# 4561096
iBlot™ 2 Transfer Stacks, PVDF, mini	Thermo Fisher Scientific	Cat# IB24002
NativePAGE 3 to 12%, Bis-Tris, 1.0 mm, Mini Protein Gel, 15-well	Thermo Scientific	Cat# BN1003BOX
Formvar/Carbon 400 Mesh, Cu grids	Electron Microscopy Sciences	Cat# FCF400-Cu
Quantifoil R 1.2/1.3 300 Mesh, Gold	Electron Microscopy Sciences	Cat# Q3100AR1.3
UltrAuFoil R 1.2/1.3, 300 mesh, Gold	Electron Microscopy Sciences	Cat# Q350AR13A
Mini-Protean Electrophoresis equipment	Biorad	Cat# 1658004
PD-10 Desalting Column	Cytiva	Cat# 17-0851-01
Spark microplate reader	Tecan	N/A
FACSMelody Cell Sorter	BD	N/A

RESOURCE AVAILABILITY

Lead contact

Further information and requests for resources and reagents should be directed to and will be fulfilled by the lead contact, wu@crystal.harvard.edu.

Materials availability

All plasmids, reagents, cell lines generated in this study are available from the [lead contact](#).

Data and code availability

- Immunoblot images data and microscopy images reported in this paper will be shared by the [lead contact](#) upon request.
- All data reported in the main and supplementary data are available upon reasonable request. The electron density maps of 3.5 Å have been deposited in the Electron Microscopy Data Bank (EMDB) with accession codes EMD-40781. The atomic coordinates for caspase-1/pro-IL-18 have been deposited in the Protein Data Bank (PDB) with the accession code 8SV1. The solution NMR structure of pro-IL-18 apo has been deposited in the PDB with the accession code 8URV and Biological Magnetic Resource Bank (BMRB) with the accession code 31122.
- Any additional information required to reanalyze the data reported in this paper is available from the [lead contact](#) upon request.

EXPERIMENTAL MODEL AND SUBJECT DETAILS

Cell lines

All mammalian cells were cultured in humidified incubators at 37 °C and 5% CO₂. HEK293T cells were cultured in DMEM supplemented with 10% fetal bovine serum (FBS), Penicillin + Streptomycin, L-Glutamine and sodium pyruvate, hereafter referred to as complete DMEM (cDMEM) and cultured in tissue-culture treated 10 cm dishes or T175 tissue culture flasks (Corning). HEK293T cells were passaged using 0.25% trypsin + EDTA (Gibco). WT THP1 cells were obtained from ATCC. *CASP1*^{−/−} THP1, THP1 cells transfected with non-target sgRNA and *IL18*^{−/−} THP1 cells reconstituted with pro-IL-18 mutants (carrying C-terminal Flag tag and N-terminal Myc-tag) were described before.²⁶ THP1 cells were cultured in RPMI supplemented with 10% FBS, Penicillin + Streptomycin, L-Glutamine and sodium pyruvate, hereafter referred to as complete RPMI (cRPMI) and cultured in suspension culture in T75 or T175 tissue culture flasks (Corning). For differentiation into macrophages, THP1 cells treated with 100 ng/ml of PMA for 18 – 24h. Sf9 insect cells were grown in suspension culture in sterile glass flask in Hyclone SFX insect cell media at 28 °C and ambient CO₂ while shaking at 120 rpm.

To produce retroviral vectors to reconstitute *CASP1*^{-/-} THP1 cells with caspase variants, HEK293T cells were used as packaging cells. 2.5×10^6 HEK293T cells were seeded in a 10 cm cell culture dish. After overnight incubation at 37 °C, cells were transfected with 10 µg of pMSCV IRES EGFP caspase-1 variants of interest, 6 µg of pCL-ECO and 3 µg of pCMV-VSVG using Lipofectamine 2000 (ThermoFisher) according to the manufacturer's instructions. After 18–24 h at 37 °C, media was changed to 6 ml of fresh cRPMI and virus-containing supernatant was collected 24 h after media change. Supernatants were clarified from cellular debris by centrifugation (400 x g, 5 min) and filtered through a 0.45 µm PVDF syringe filter. 1×10^6 THP1 cells were resuspended in 4.5 ml of viral supernatant supplemented with Polybrene (1:2000; EMD Millipore) and plated in a 6-well plate followed by centrifugation for 1 h at 1250 x g and 30 °C. Cells were transduced twice on two consecutive days to maximize transduction efficiency. GFP⁺ cells were sorted twice on a FACSMelody cell sorter (BD Biosciences) to obtain cell lines with stable and homogenous expression of the target protein. Transgene expression was confirmed by immunoblotting using a rabbit anti-Myc-tag primary antibody (Cell Signaling Technologies).

METHOD DETAILS

Construct design

The constructs encoding the large (p20) and small (p10) subunits of human caspase-1 were kindly provided by Sam Xiao (Case Western Reserve University).³⁹ The construct encoding the caspase-1 catalytically inactive mutant of p20 (C285A) was kindly provided by Feng Shao (National Institute of Biological Sciences).³⁵ The pET21b-Casp1-His plasmid containing human full-length caspase-1 (Addgene) was used as a template to subclone p33, p22, or p12 into the pET21a vector without a fusion tag to generate active forms of caspase-1 truncation. Additionally, p33, p22, or p12 fragments were subcloned to pET28a vector with N-terminal 6xHis-SUMO tag, further introduced with C285A mutation to generate inactive forms. The quadruple mutations D92A/D103A/D119A/E130A were introduced to the p33 construct to prevent the self-cleavage between CARD and the p20 subunit. The double mutations D297A/D315A were introduced to the p22 construct to prevent the p20-generating self-cleavage at the IDL. The double mutations D315A/D316A were introduced to the p12 construct to prevent the p10-generating self-cleavage at the IDL. The constructs encoding human caspase-1 p20 (active and inactive forms) and p10 subunits were used as a template to further introduce site mutations for validating the binding interface of the caspase-1/pro-IL-18 complex. The constructs encoding human pro-IL-18 and pro-IL-37 carrying a C-terminal Myc-tag were generated previously.²⁶ The construct encoding human pro-IL-18 was cloned into a pET28a vector with an N-terminal 6xHis tag. The construct encoding human pro-IL-1β was cloned into the pFastBac vector with an N-terminal 6xHis-SUMO tag. pMSCV-EGFP vector encoding N-terminally Myc-tagged human caspase-1 was described before⁴² and is available on Addgene (#183359). All site-directed mutations were introduced by using the Q5 site-directed mutagenesis kit (NEB).

Cell-based NLRP3 inflammasome assays and immunoprecipitation of IL-1 cytokines

THP1 cells were differentiated with 100 ng/ml of PMA in cRPMI for 18–24 h (1×10^5 cells in 200 µl per well in a 96-well plate), then primed with 1 µg/ml of LPS for 4 h before stimulating them with 20 µM of nigericin for 2–3 h. LDH release into the supernatants was measured using the CyQuant LDH cytotoxicity assay (Thermo Fisher) and IL-18 or IL-1β amounts were quantified by ELISA (kits from R&D Systems). To measure IL-18 amounts in combined supernatants and cell lysates, cells were lysed by adding 20 µl of detergent-containing lysis buffer to each well (provided with CyQuant LDH assay kit).

To analyze cellular cytokine processing, IL-1β and IL-18 were immunoprecipitated from the supernatants of LPS + Nigericin stimulated THP1 macrophages. 2×10^6 THP1 cells were seeded in 6-well plates in 2 ml of cRPMI + 100 ng/ml PMA for 18–24 h. Cells were then primed with 1 µg/ml of LPS for 4 h before stimulating them with 20 µM of nigericin for 2–3 h. Supernatants were cleared of floating cells by centrifugation at 400 g at 5 min. Cell-free supernatants were transferred into new tubes and rotated overnight at 4 °C in the presence of 0.5 µg of biotinylated goat anti-human IL-1β antibodies or 0.25–0.75 µg of detection antibodies from human IL-18 ELISA kit (all from R&D Systems) and 20 µl neutravidin agarose beads (Thermo Fisher). IL-18 mutant proteins carrying C-terminal Flag-tags, were immunoprecipitated using 15 µl of Anti-Flag matrix (Thermo Fisher). The remaining cells were lysed in 1x SDS loading dye and served as lysate control. Beads were washed three times with PBS pH 7.4 before eluting bound proteins in 50 µl of 1x SDS loading dye. Immunoprecipitated and cell-associated cytokines were detected by immunoblotting using rabbit anti-human IL-1β antibody (Genetex), rabbit anti-human IL-18 antibody (MBL). Cell-associated actin was detected as a loading control using a mouse anti-actin antibody from Sigma.

Protein expression and purification

The expression and purification of the catalytically active caspase-1 including all the auto-processed forms and site mutations were performed by using a protocol adapted from the previously refolding method.⁶⁷ Basically, two non-tagged large and small subunits were transformed in *E. coli* BL21 (DE3) respectively. 0.5 L bacteria culture for large and small subunits were grown respectively at 37 °C and induced with 0.5 mM isopropyl β-D-1-thiogalactopyranoside (IPTG) 4 hrs. at 37 °C after OD600 reached 0.8. The bacteria were lysed and centrifuged at 17,000 g for 30 min. The collected pellets were washed twice with 0.1% Triton-X-100 in buffer A containing 50 mM Tris-HCl (pH 8.0), 300 mM NaCl, and 1 M guanidinium hydrochloride (GdnCl). The pellets were then cleaned up to remove 0.1% Triton-X-100 by washing twice with buffer A. The inclusion bodies were incubated in buffer B containing 6 M GdnCl, 25 mM Tris-HCl (pH 7.5), 5 mM EDTA, and 100 mM TCEP to achieve a final volume of 6 ml and solubilized overnight. The 6 ml mixture was diluted into 250 mL of buffer C containing 100 mM HEPES (pH 8.0), 100 mM NaCl, 100 mM sodium malonate, 20% sucrose,

0.5 M NDSB-201 and 10 mM TCEP, followed by centrifugation at 17,000 g for 30 min. The supernatant was concentrated to 60 ml and dialyzed overnight over buffer D containing 30 mM sodium acetate (pH 5.9), 5 mM TCEP, and 5% (v/v) glycerol. The assembled complex was further purified by using HiTrap SP cation exchange chromatography (GE Healthcare Life Sciences) with buffer E containing 30 mM sodium acetate (pH 5.9), 1 M NaCl, 5 mM TCEP, and 10% (v/v) glycerol.

The expression and purification of the catalytically inactive caspase-1 including all the auto-processed forms and site mutations were performed using soluble expression. Plasmids of large and small subunits were co-transformed in an equal ratio into *E. coli* BL21 (DE3) respectively. The bacteria with the co-expression of both large and small subunits were cultured in LB medium and induced overnight at 18°C with 0.5 mM IPTG after OD600 reached 0.8. The harvest bacteria were lysed in buffer F containing 20 mM Tris-HCl (pH 8.0), 300 mM NaCl, and 1 mM TCEP, with the addition of EDTA-free Protease Inhibitor Cocktail (Sigma Aldrich), followed by centrifugation at 17,000 g for 30 min. The assembled proteins were purified by using Ni-Sepharose beads (GE Healthcare Life Sciences). The eluted protein was digested with home-made SUMO protease to remove the 6xHis-SUMO tag followed by dialyzing against buffer D. The supernatant was filtered and subjected to HiTrap SP cation exchange column for further purification against buffer E.

The wild-type (WT) pro-IL-18 and pro-IL-1 β protein was expressed in sf9 insect cells by using a baculovirus expression system (Thermo Scientific) and purified as described.²⁶ Pro-IL-1 β was expressed and purified using equivalent protocols. The N-terminal 6xHis-SUMO tag at pro-IL-1 β was removed by adding homemade SUMO protease at a ratio of 1:50 (w/w) for pro-IL-1 β and SUMO protease and incubating overnight at 4°C, before performing the further gel filtration shift assay. The pro-IL18 double mutation (V147NN and E192KK), and triple-peptide mutation (LES33AAA) were expressed in *E. coli* BL21 (DE3) respectively. The bacteria culture was grown at 37°C and induced overnight at 18°C with 0.5 mM IPTG after OD600 reached 0.8. The bacteria pellets were harvested and lysed by using buffer F with EDTA-free Protease Inhibitor Cocktail, followed by centrifugation at 17,000 g for 30 min. The supernatant was collected and purified by using Ni-Sepharose beads in buffer F. The fusion protein was eluted from the Ni-NTA beads with buffer F containing 200 mM imidazole and purified by Superdex 200 10/300 GL size-exclusion column (GE Healthcare Life Sciences) in the buffer G containing 20 mM HEPES pH 7.5, 150 mM NaCl, and 1 mM TCEP. The eluted protein was digested with homemade TEV protease to remove the 6xHis tag. Pro-IL-37 was expressed and purified from bacteria with similar procedures as pro-IL-18. GSDMD was expressed and purified by following the previous protocol.⁹

Caspase-1 and pro-IL-18 complex assembly

The purified caspase-1 p20/p10 (C285A) and pro-IL-18 were mixed at 37°C for 20 min at 1:2 molar ratio to facilitate the formation of complex. The mixture was centrifuged at 20,000 g for 10 min and subjected to Superdex 200 10/300 GL size-exclusion column in buffer G to separate the well-assembled caspase-1/pro-IL-18 complex. The peak from the gel filtration was collected and cross-linked with 1 mM bis (sulfosuccinimidyl) suberate (BS3) (Thermo Scientific) for 1 h at room temperature. The reaction was quenched by adding a final concentration of 50 mM Tris-HCl and further purified by gel filtration. The assembled complex was further checked by negative staining EM and cryo-EM sample preparation (see below).

Negative staining EM

The peak fractions from gel filtration of caspase-1/pro-IL-18 complex were diluted to a final concentration of 0.01 mg/ml for negative staining EM. 6 μ l sample was subjected to a copper grid with carbon support film (Electron Microscopy Sciences) glow discharged for 30 seconds using a Pelco EasyGlow (Ted Pella) instrument. The sample was incubated for 1 min before being stained by 6 μ l 2% uranyl acetate solution (Electron Microscopy Sciences) twice for 30 seconds each. The filter papers (Whatman) were used to remove excess buffer during the staining steps. The sample of the negatively stained grids were imaged on a Transmission Electron Microscope (Joel JEM1400) at 120 keV.

Cryo-EM data collection

The peak fractions of crosslinked caspase-1/pro-IL-18 complex from gel filtration were concentrated to a final concentration of 0.15 mg/ml for cryo-EM sample preparation. 3.3 μ l of the protein samples were placed onto glow-discharged cryo-EM grids before being blotted for 3–5s under 100% humidity at 4 °C and plunged into liquid ethane using a Mark IV Vitrobot (ThermoFisher). Quantifoil R1.2/1.3, gold grids with 400 mesh (Electron Microscopy Sciences), and Quantifoil® UltrAuFoil Gold Hole Carbon Films R1.2/1.3 with 300 mesh (Electron Microscopy Sciences) were used for un-tilted or tilted data collection respectively. Before data collection, all the grids were pre-screened and optimized at the cryo-EM facility of the University of Massachusetts (UMASS), Harvard Cryo-EM Center for Structural Biology (HMS), and Pacific Northwest Center for Cryo-EM at Oregon Health & Science University (PNCC) to check the thickness of the ice and distribution of the particles.

The final datasets were collected in two separate sessions at two tilt angles. The first dataset was collected at UMASS on a Titan Krios electron microscope (Thermo Fisher Scientific) equipped with a K3 Summit direct electron detector (Gatan) and a post-column energy filter (Gatan). 4,437 movies were collected at 0° tilt angle under the super-resolution mode with 105,000 \times magnification (0.4125 Å per pixel) with a defocus range varying between -1.0 and -2.5 μ m and to record three shots for each hole per stage movement. For each image stack with 40 frames, the total dose was 55.4 electrons per Å². The second dataset was collected at HMS using a Titan Krios microscope (ThermoFisher) operating at an acceleration voltage of 300 keV equipped with BioQuantum K3 Imaging Filter (Gatan, slit width 20 eV). 3,240 movies were collected under the super-resolution mode with 105,000 \times magnification (0.4125 Å per pixel) with a defocus range varying between -0.8 and -1.8 μ m and to record one shot for each hole per stage movement with a 30° tilt

angle, as suggested by cryoEF analysis.³⁸ For each image stack with 40 frames, the total dose was 55.4 electrons per Å.² SerialEM was used for automated data collection.

Cryo-EM data processing

SBGrid consortium⁵⁹ provided the computer support and software for data processing support. For the dataset collected at 0° tilt angle, raw movies were corrected by gain reference and beam-induced motion by binning twofold with or without dose weighting using the Relion 3.08 implementation of the MotionCor2 algorithm.⁵⁴ The motion-corrected micrographs were imported into cryo-SPARC.⁶⁸ Patch CTF estimation was performed to determine the defocus value of each micrograph. Blob picking on a random subset of 500 micrographs was used to generate a template used for further picking a total number of 4,218,303 particles. Several rounds of 2D classification were performed to select 468,584 good particles for further ab initio reconstruction to generate initial models. The initial models were processed with heterogeneous refinement to classify the particles into five classes. Two major classes appeared indicating proximal and distal conformations, with 141,806 and 129,328 particles individually. The two classes are further processed by homogeneous refinement with C1 symmetry to achieve 4.2 and 4.0 Å resolution maps for proximal and distal conformations, respectively. However, orientation preference appeared in both maps.

For the dataset collected at a 30° tilt angle, motion correction was processed similarly as 0° tilt angle. The motion-corrected and CTF-refined micrographs were used for particle picking. By using the template generated from the 0° tilt angle dataset, 2,811,641 particles were picked for further 2D classification. After several rounds of 2D classification, 329,763 particles were selected for ab initio reconstruction followed by heterogeneous refined with C1 symmetry. The map showed imprecision of contrast-transfer function (CTF) estimation indicated by the strong fluctuations of the Fourier shell correlation (FSC) curve. Local CTF refinement was performed to rectify for per-particle defocus. A total number of 440,340 refined particles from 0° and 30° tilt angles were combined for several rounds of heterogeneous refinement to select 206,959 good particles. Homogeneous refinement was performed with C2 symmetry to achieve 3.5 Å map. The reported resolutions were estimated based on the gold-standard Fourier shell correlation (FSC) = 0.143 criterion. The cryo-EM map for proximal conformation was corrected and sharpened by applying a negative B factor using automated procedures in Phenix.⁶⁹ 3D variability analysis (3DVA)⁵² of caspase-1 and pro-IL-18 complex were processed in CryoSPARC. Local resolution estimation of all the cryo-EM maps was estimated in CryoSPARC.

Model fitting and building

The crystal structure of caspase-1 dimer (PDB: 6KNO)³⁹ and IL-18 (PDB: 3WO2)⁴⁰ were used as templates for fitting. The initial model fitting into the cryo-EM map was performed in UCSF ChimeraX.⁷⁰ The tetrapeptide sequence (33-LESD-36) of pro-IL-18 was manually built at active site. The model building of the majority part of pro-IL-18 pro-domain, and connecting to the rest part of IL-18 were performed by COOT.⁵⁷ The structure of caspase-1 and pro-IL-18 complex was refined by real-space refinement and validated by model validation in Phenix.^{58,69} Interaction analysis was conducted by using PISA.⁴¹ Per residue Cα–Cα distances between caspase-1 and pro-IL-18 in the complex were calculated with the Distances function in UCSF ChimeraX.⁵³ Model alignments were carried out in the matchmaker module in UCSF Chimera. The model schematics were created with BioRender.com.

Crosslinking mass spectrometry

The caspase-1/pro-IL-18 complex was crosslinked by BS3 and quenched by hydroxylamine (Sigma Aldrich) to achieve a final concentration of 100 mM. The mixture was subject to gel filtration to exchange into buffer H containing 20 mM HEPES pH 7.5, and 150 mM NaCl. The complex was concentrated to a final concentration of 0.15 mg/ml for further crosslinking mass spectrometry analysis as the previously described method.⁷¹

Immunoblotting

All the samples were run with 4–15% or 4–20% Mini-Protein Precast Protein Gels (BIO-RAD) for 25–40 min at 180V. Gels were transferred to PVDF or nitrocellulose membrane (Fisher Scientific) with the iBlot 2 Gel Transfer Device (Invitrogen). Primary antibodies for immunoblotting used in this study include monoclonal rabbit anti-human caspase-1, monoclonal rabbit anti-Myc tag, monoclonal rabbit anti-murine IL-18 (all from Cell Signaling), polyclonal rabbit anti-human IL-18 (MBL), polyclonal goat anti-human IL-1β (R&D Systems) and monoclonal mouse anti-β-actin (Sigma Aldrich).

In vitro protein cleavage assay

Proteolytic cleavage of purified full-length protein substrates by caspases was assessed as described before.^{33,34} Active site titrations with the inhibitor zVAD-fmk were performed as described previously to determine the concentration of active caspase in each protein preparation.⁷² Two-fold dilution series of the indicated recombinant caspase was incubated with substrate protein at a final concentration of 50 nM in 40 μl of caspase assay buffer (10 mM PIPES pH 7.2, 10% sucrose, 10 mM DTT, 100 mM NaCl, 1 mM EDTA, 0.1% CHAPS) for 30 min at 37°C. Reactions were stopped by adding 10 μl of 5x SDS loading dye with a reducing agent and boiling at 65°C for 10 min. Cleavage products were separated by SDS-PAGE and analyzed via immunoblotting using rabbit anti-human IL-18 (MBL), rabbit anti-murine IL-18 (Abcam), rabbit anti-Myc (Cell Signaling), rabbit anti-human IL-1β (Genetex) or rabbit anti-GSDMD (Cell Signaling) primary antibodies. Band intensities were quantified using ImageJ to determine EC50 values and catalytic efficiencies were calculated using the following equation:

$$\frac{k_{cat}}{K_m} = \frac{\ln(2)}{(EC_{50} \times t)}$$

In vitro peptide cleavage assay

For peptide cleavage assays, recombinant caspase-1 variants were diluted to a concentration of 100 nM in caspase assay buffer (active caspase concentration as determined by active site titration). To start the reaction, 50 μ l of the diluted caspase was then mixed with 50 μ l of the chromogenic tetrapeptide substrate Ac-WEHD-pNA (100 μ M final concentration) in the same buffer (final concentration of caspase was 100 nM in a total volume of 100 μ l) in a clear 96-well plate. Absorbance at a wavelength of 405 nm was measured every 10 s for 30 min using a Tecan Spark plate reader with temperature control set to 37°C. Substrate solution was pre-warmed to 37°C before adding to the caspase to ensure homogeneous assay conditions.

Gel filtration shift assay

To evaluate the binding between caspase-1 and pro-IL-18 or pro-IL-1 β , a gel filtration shift assay by size exclusion chromatography (SEC) was performed. 200 μ l of 20 μ M catalytically inactive caspase-1 and 50 μ l of 150 μ M pro-IL-18 variants were mixed at (1:2 molar ratio) in SEC buffer (25 mM HEPES pH 7.4, 150 mM NaCl) with excess pro-IL-18 to allow the saturation of caspase-1. After incubation at 37°C for 20 min, gel filtration was performed on an AKTA Chromatography system equipped with a Superdex 200 Increase 10/300 column.

Cloning, expression, purification, and sample preparation for NMR studies

Isotopically enriched samples of pro-IL-18 ([U - ^{13}C , ^{15}N]- and [U -5%- ^{13}C , 100%- ^{15}N]-pro-IL-18) were expressed and purified from *E. coli*. Briefly, the 193-residue coding sequence of pro-IL-18 was cloned into the Champion pET SUMO vector (ThermoFisher Scientific) in frame with an N-terminal 6x His and SUMO tag, transformed into *Escherichia coli* BL21 (DE3) cells, and expressed in M9 minimal medium containing either U - $^{15}\text{NH}_4\text{Cl}$ and U - ^{13}C -glucose as the sole nitrogen and carbon sources for the production of a U - ^{13}C , ^{15}N sample or U - $^{15}\text{NH}_4\text{Cl}$ and 5% U - ^{13}C -glucose/95% ^{12}C -glucose for generating [U -5%- ^{13}C , 100%- ^{15}N]-pro-IL-18. Initial cell growth was carried out at 37°C, and protein expression was induced at 25°C by 0.1 mM IPTG at an OD_{600} of 0.8 and continued for 20 hours. Protein purification was carried out at room temperature using 20 mM Tris buffers at pH 8. Cells were lysed by sonication on ice in the presence of 0.5 M NaCl and a trace of DNase I. Clarified cell extracts were loaded onto a Ni-NTA column, purified by a wash step with 10 mM imidazole, and then the 6x His labeled protein was eluted using 0.3 M imidazole. The 6x His and SUMO tags were then cleaved by homemade Ulp1 protease during an overnight dialysis step to remove the imidazole, in the presence of 0.1 M NaCl. A second Ni-NTA step was performed in which the tag-less pro-IL-18 is found in the flow-through. Subsequently, pro-IL-18 was subjected to size exclusion chromatography using a prepacked 16/600 Superdex 75 column in the presence of 50 mM NaCl. The final yield of purified isotopically-enriched pro-IL-18 was approximately 22 mg/L of culture. Sample purity and molecular mass were confirmed by SDS-PAGE and mass spectrometry. Samples of [U - ^{13}C , ^{15}N]- and [U -5%- ^{13}C , 100%- ^{15}N]-pro-IL-18 for NMR spectroscopy were concentrated by ultracentrifugation to 0.5 mM in 20 mM MES, 50 mM NaCl, and 10 mM DTT at pH 6.5, and 3% D_2O was added to each sample. In contrast, the sample for recording the ^{13}C -edited NOESY was in 99.8% D_2O and pD (uncorrected) was 6.1.⁷³

NMR spectroscopy

NMR experiments were collected at 25°C on Bruker AVANCE NEO 23.5 T (1.0 GHz) and AVANCE III HD 18.8 T (800 MHz) and 14.1 T (600 MHz) NMR spectrometers equipped with 5-mm TCI triple-axis gradient cryoprobes. The recorded data were processed with NMRpipe,⁷⁴ and analyzed using NMRFAM-SPARKY.⁷⁵ Automated backbone resonance assignments were made using I-PINE,⁷⁶ based on peak lists from gradient-enhanced sensitivity 2D ^1H - ^{15}N HSQC⁷⁷ and 3D HNCO, HN(CA)CO, C(CO)NH and HNCACB⁷⁸ spectra, and were validated by manual inspection of an HNN spectrum.⁷⁹ Side chain assignments were completed manually using 3D HBHA(CO)NH,⁸⁰ as well as H(CO)NH, C(CO)NH experiments,⁸¹ and a C(CA)NH TOCSY experiment derived from the C(CO)NH. Stereospecific isopropyl methyl resonance assignments for all Val and Leu residues were determined from a constant time ^1H - ^{13}C HSQC spectrum recorded on [U -5%- ^{13}C]-pro-IL-18,⁸² with a constant-time delay of 28 ms during which ^{13}C chemical shift is recorded.^{83,84} Aromatic side chain assignments were obtained from 2D (HB)CB(CGCD)HD and (HB)CB(CGCDCE)HE experiments⁸⁵ and confirmed with a short mixing time ($\tau_m = 40$ ms) 2D NOESY dataset. Methionine methyl assignments were deduced from a 2D long-range ($\text{C}^\beta/\text{C}^\gamma \rightarrow \text{C}^\delta$) J-correlation experiment.⁸⁶ Sidechain χ_1 dihedral angles for Ile, Thr, Val, and aromatic (Phe and Tyr) residues were derived from three-bond ^{13}C - ^{13}C CO and ^{13}C - ^{15}N couplings where j is either a methyl carbon^{87,88} or an aromatic C^γ carbon.⁸⁹ Interproton distance restraints for structure determination were obtained from 3D gradient-enhanced⁷⁷ $\{^1\text{H}, ^{15}\text{N}, ^1\text{H}\}$ and $\{^{15}\text{N}, ^{15}\text{N}, ^1\text{H}\}$ NOESY-HSQC experiments,⁹⁰ and a 3D $\{^1\text{H}, ^{13}\text{C}, ^1\text{H}\}$ NOESY-HSQC dataset⁹¹ recorded in D_2O , all acquired with a mixing time of 150 ms, 23.5 T. All 3D experiments were obtained using non-uniform sampling (NUS) with a Poisson-Gap sampling schedule,⁹² and reconstructed using the SMILE algorithm⁹³ within NMRPipe.

In order to assess the mobility of the pro-IL-18 backbone at each amide site we have measured ^{15}N longitudinal (R_1) and $R_{1\rho}$ relaxation rates, with ^{15}N R_2 values calculated as⁹⁴

$$R_2 = \frac{R_{1\rho}}{\sin^2 \theta} - \frac{R_1}{\tan^2 \theta} \quad [\text{Equation 1}]$$

In Equation 1 $\sin \theta = \frac{\omega_1}{\sqrt{\omega_1^2 + \Omega^2}}$ and $\tan \theta = \frac{\omega_1}{\Omega}$, with ω_1 and Ω the spin-lock power and the offset of the ^{15}N spin in question from the ^{15}N carrier frequency, respectively. ^{15}N spin relaxation measurements were recorded with pulse sequences similar to those in Farrow et al.,⁹⁵ with the exception that a spin-lock element was used to measure $R_{1\rho}$ rates rather than refocused free-precession of magnetization from which R_2 rates are obtained. A series of 2D datasets were recorded with delays of (0.01, 0.25, 0.5, 1.0, 1.5) s and (5, 10, 15, 20, 25, 30, 35, 40, 45, 50, 55, 65, 75) ms for R_1 and $R_{1\rho}$ measurements, respectively, and a ^{15}N spin lock power of 2,000 Hz ($R_{1\rho}$). These experiments were recorded at 23.5 T.

Solution NMR structure refinement

The solution NMR structure of the apo-form of pro-IL-18 was calculated using the latest version of CYANA (3.98.15)^{60,61} supplied with peak intensities from NOESY-HSQC spectra detailed above, together with dihedral angle constraints derived from TALOS+⁶² ($\phi, \psi \pm 20^\circ$ or 30° based on the TALOS+ analysis results) restricted to residues with confidence scores of 10 and only in secondary structural elements. NMR-derived χ_1 dihedral angle restraints ($\pm 30^\circ$) were added to the calculations in the final stages of the structure determination. Automated NOESY assignment CYANA structure calculations were performed with an upper distance bound limit set to 6.0 Å over seven cycles, in which the 20 lowest target function structures out of 100 were retained per cycle. The best 10 structures from the final cycle of CYANA were further refined using restrained energy minimization following the Rosetta FastRelax protocol^{96,97} using Rosetta version 3.12 running in NMRbox.⁶⁶ The ramp_constraints flag was set to false to preserve the constraints throughout the entirety of the minimization. PdbStat⁶³ was used to convert coordinates, distance, and dihedral angle restraints from CYANA to the Rosetta3 format, and upper distance bounds were increased by 20%, and those within disordered (loop) regions of the structure increased by an additional 1.0 Å. Distance and dihedral restraints were applied in Rosetta using harmonic and circular harmonic functions, respectively, with a weight of 1.0. Each of the 10 final CYANA structures was subjected to 10 restrained Rosetta relax calculations, and the lowest energy structure from each calculation was retained to produce the final ensemble of 10 pro-IL-18 structures reported. For one of the final CYANA structures, the second lowest energy structure of the 10 relax calculations was used in the ensemble in order to keep the tautomerization state of H145 consistent across each structure in the ensemble. Structural statistics and global structure quality factors were obtained from the PSVS 2.0⁶⁴ and MolProbity⁶⁵ servers (Table S2).

QUANTIFICATION AND STATISTICAL ANALYSIS

No statistical methods were used to predetermine sample size. GraphPad Prism software was used for data analysis. The data shown are representative of three independent experiments. Bars and error bars represent the mean \pm SEM of at least three independent experiments. Statistical significance was determined by one-way ANOVA with Tukey's multiple comparisons test: ** $p < 0.01$; *** $p < 0.001$; **** $p < 0.0001$.

Immunity, Volume 57

Supplemental information

Structural transitions enable interleukin-18 maturation and signaling

Ying Dong, Jeffrey P. Bonin, Pascal Devant, Zhuoyi Liang, Alexander I.M. Sever, Julian Mintseris, James M. Aramini, Gang Du, Stephen P. Gygi, Jonathan C. Kagan, Lewis E. Kay, and Hao Wu

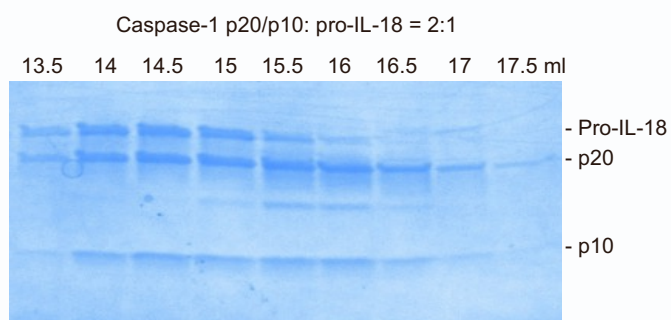
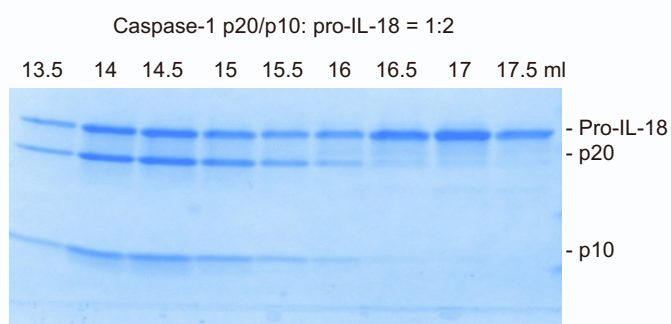
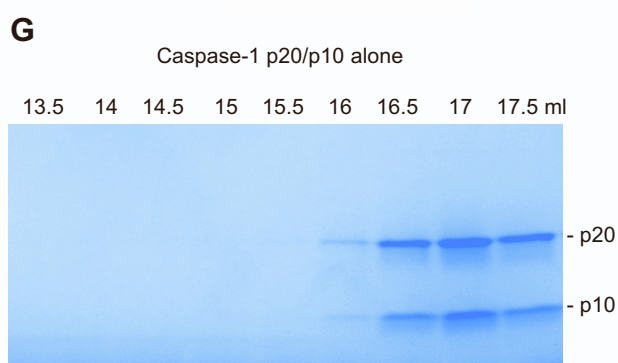
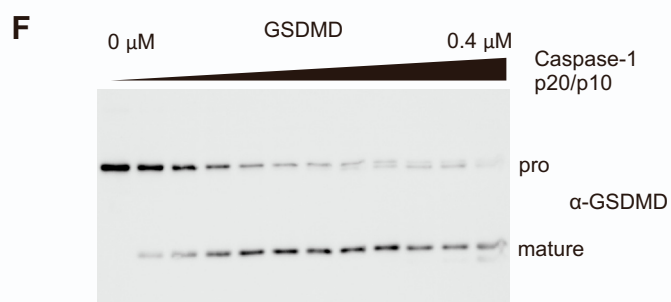
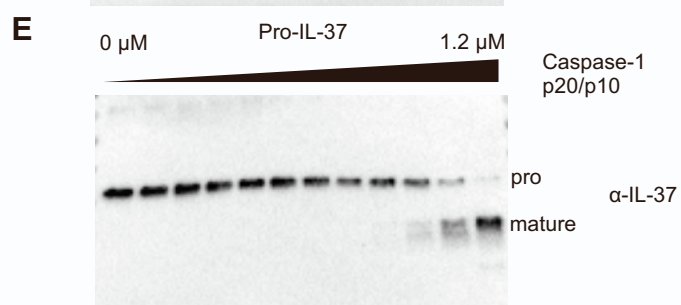
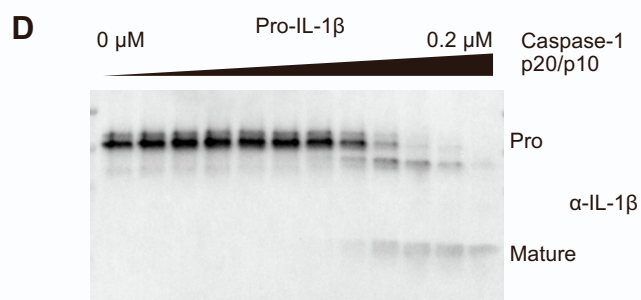
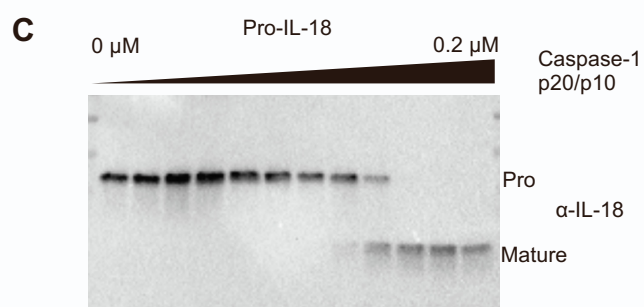
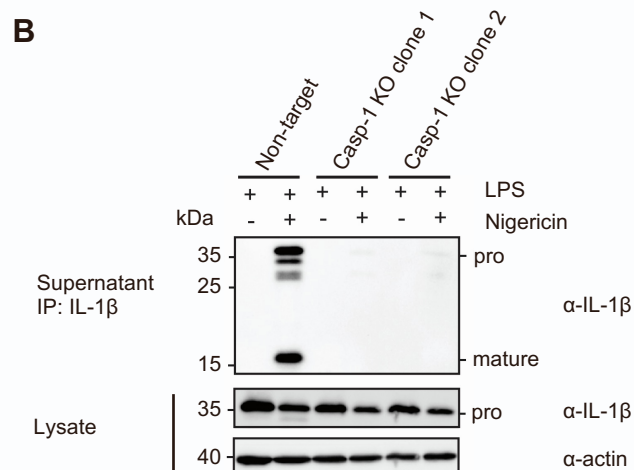
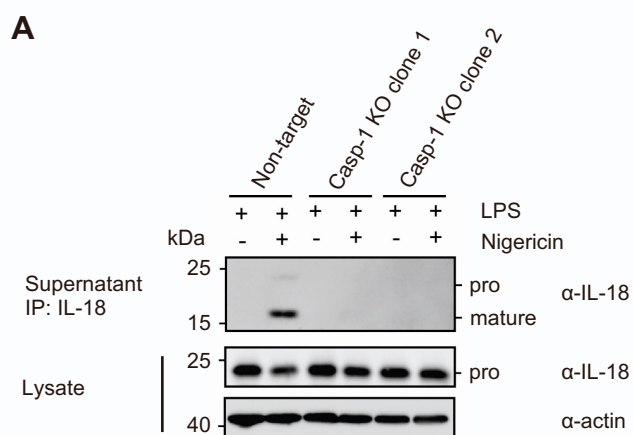


Figure S1. Biochemical characterization for the processing of different substrates by human caspase-1, related to Figure 1

(A,B) Immunoblots for the non-target control and two clones (shown as clones 1 and 2) of caspase-1 knockout (KO) THP-1 macrophages primed with LPS for 4 h before treatment with nigericin for 2-3 h. IL-18 (A) and IL-1 β (B) were immunoprecipitated from cell culture supernatants and analyzed by immunoblot.

(C-F) Immunoblots showing *in vitro* catalytic efficiency of caspase-1 on pro-IL-18 (C), pro-IL-1 β (D), pro-IL-37 (E) and GSDMD (F). The concentrations displayed are active caspase-1 concentrations determined by active site titration assay, and are 2-fold dilution series.

(G) The SDS-PAGE of gel filtration fractions of caspase-1 p20/p10 (C285A catalytic mutant) alone, caspase-1 p20/p10 (C285A catalytic mutant) and pro-IL-18 mixed at 1:2 or 2:1 molar ratios, indicating that pro-IL-18 can dimerize caspase-1 p20/p10 at a substoichiometric ratio. The elution volume of individual fractions from a Superdex 200 column are indicated.

The data shown are representative of at least three independent experiments.

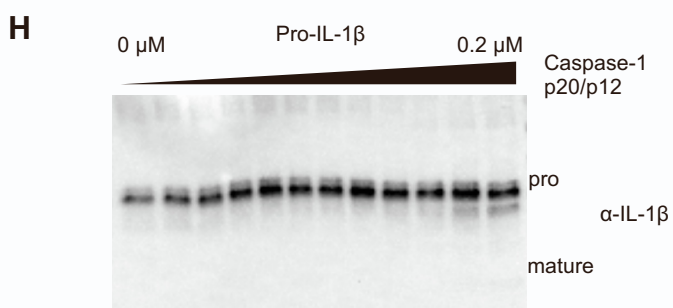
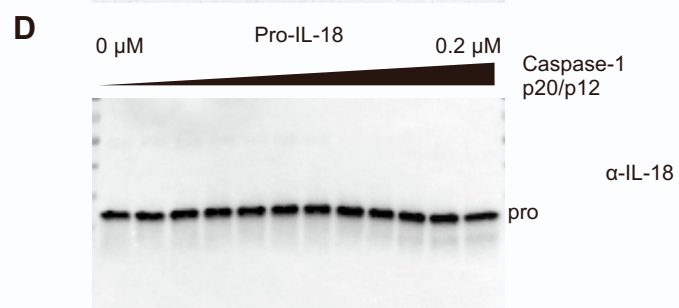
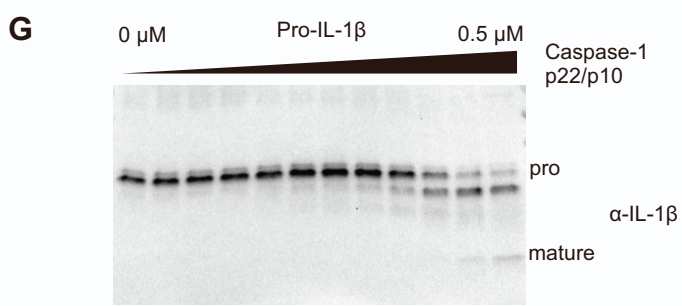
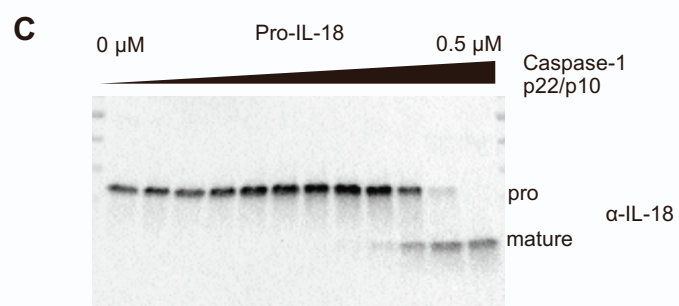
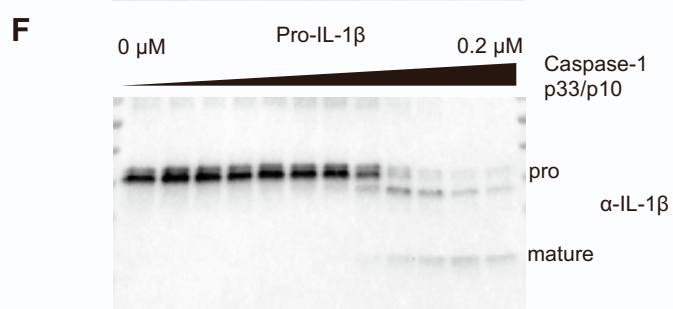
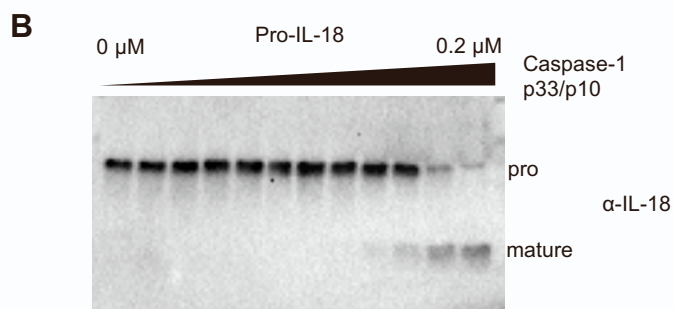
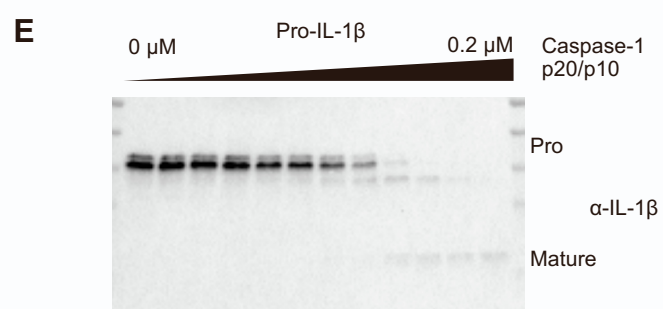
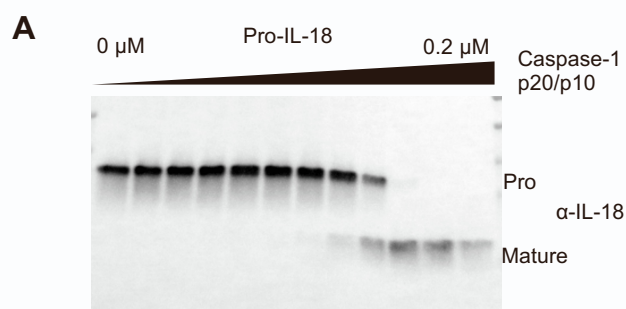
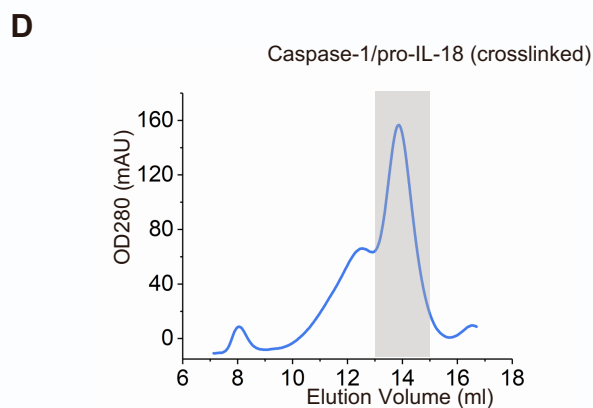
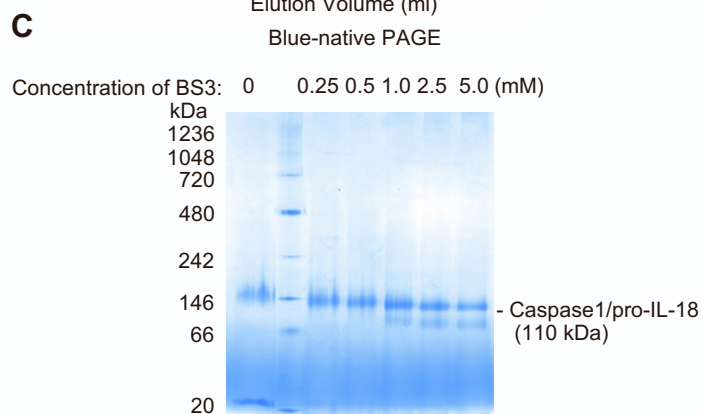
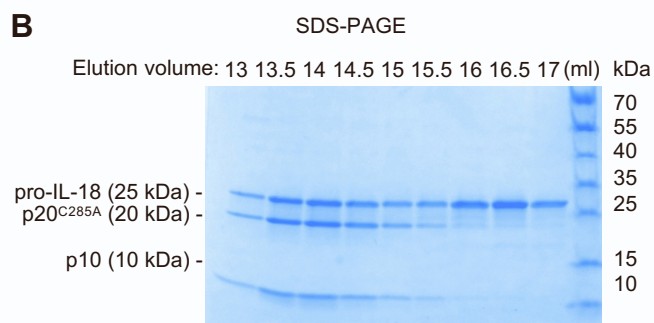
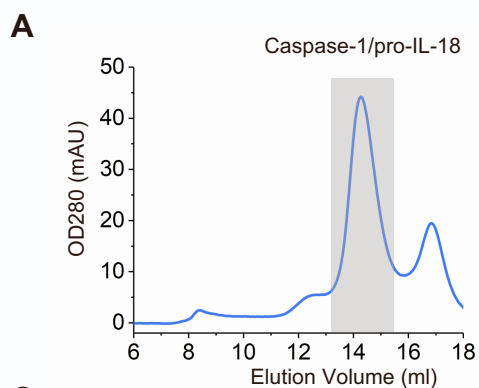


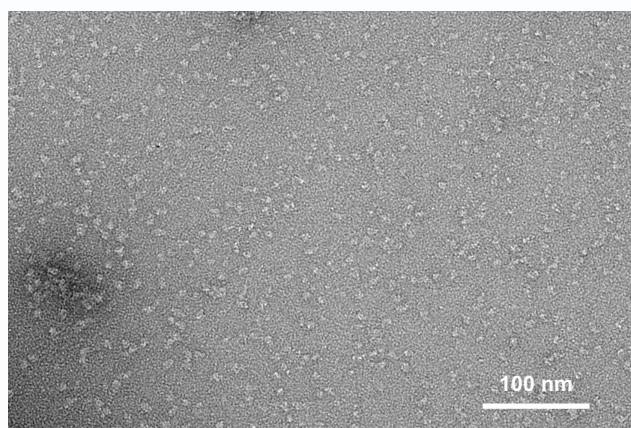
Figure S2. Biochemical characterization for the processing of pro-IL-18 and pro-IL-1 β by different auto-processed forms of human caspase-1, related to Figure 2

(A-H) Immunoblots showing *in vitro* catalytic efficiency determination of indicated auto-processed forms of caspase-1 on pro-IL-18 (A-D) and pro-IL-1 β (E-H). The concentrations displayed are active caspase-1 concentrations determined by active site titration assay, and are 2-fold dilution series. The data shown are representative of three independent experiments.



E

Negative staining raw image of caspase-1/pro-IL-18



F

Cryo-EM raw image of caspase-1/pro-IL-18

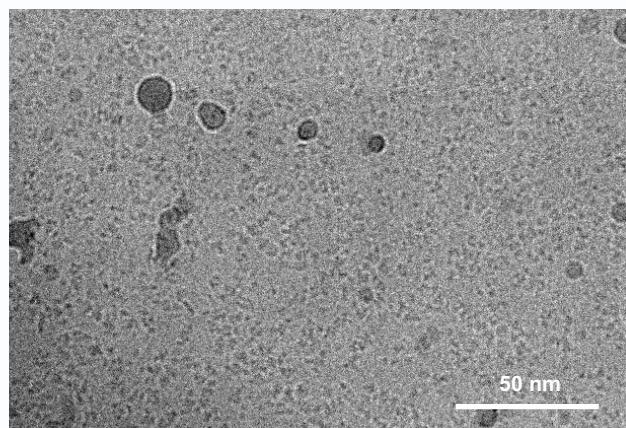
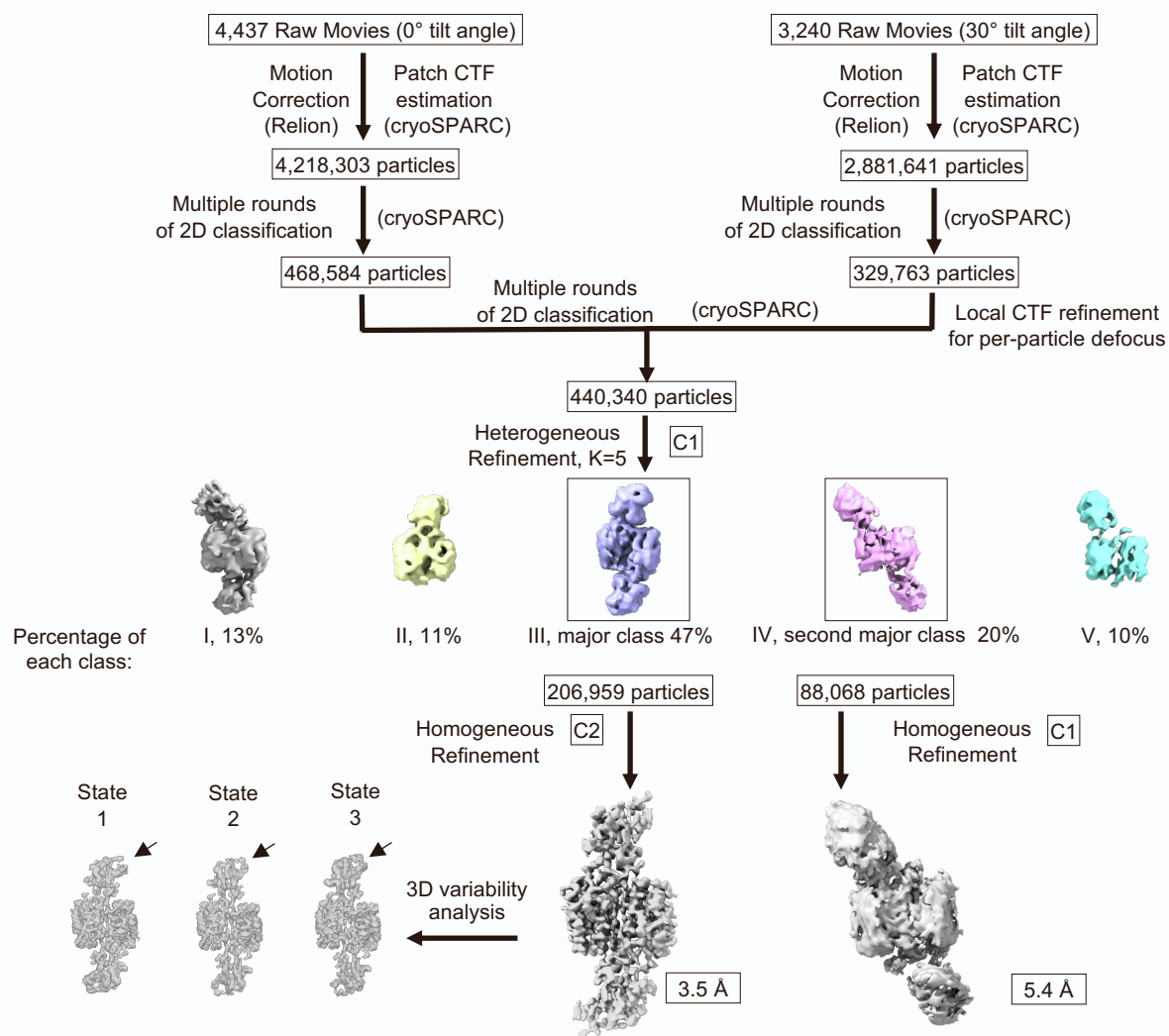
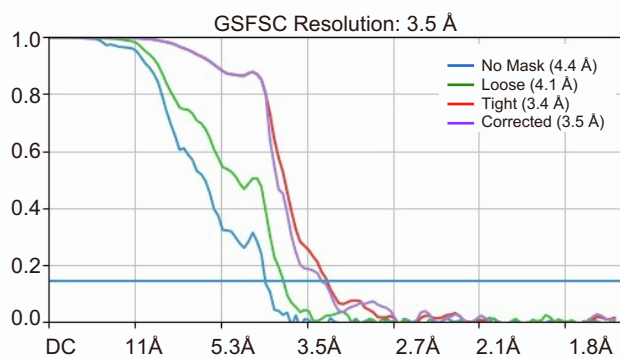
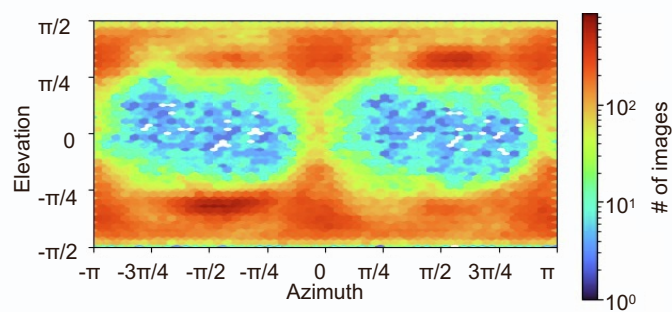


Figure S3. Preparation of the caspase-1/pro-IL-18 complex, related to Figure 3

- (A) Gel filtration profile of the caspase-1/pro-IL-18 complex before crosslinking. The major peak collected for further biochemical analysis and cryo-EM sample preparation is indicated in the gray area.
- (B) SDS-PAGE gel of fractions from the gel filtration chromatography in (A).
- (C) Blue-native (BN) PAGE of the caspase-1/pro-IL-18 complex crosslinked by different concentrations of BS3 ranging from 0 - 5 mM.
- (D) Gel filtration profile of the caspase-1/pro-IL-18 complex from the peak in (A) crosslinked by 1 mM BS3.
- (E) Representative negative staining image of the caspase-1/pro-IL-18 complex.
- (F) Representative cryo-EM raw image of the caspase-1/pro-IL-18 complex.

A**B****C****D**

Caspase-1/pro-IL-18 (color code consistent with Fig.3E-F) and Caspase-4/pro-IL-18 (color in gray) alignment at caspase region

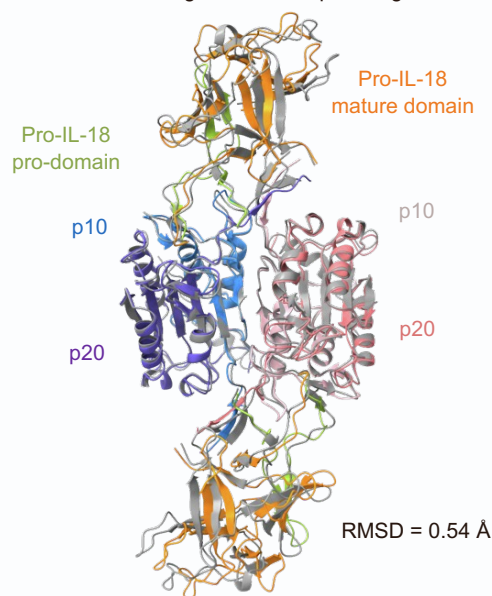


Figure S4. Cryo-EM data processing for caspase-1 and pro-IL-18 complex, related to Figure 3

(A) Cryo-EM data processing flow chart. The heterogeneous refinement results in five representative classes. The percentage of each class is shown. The major class and second major class are highlighted. The homogeneous refinement was performed with (C2) or without (C1) symmetry to obtain the final map for the two major classes. The 3D variability analysis was performed in CryoSPARC and showed three representative states from the major class. The flexible region of pro-IL-18 revealed by the 3D variability analysis is indicated by an arrow.

(B) Gold-standard FSC curves of the major class between two half maps, unmasked (blue), loosely masked (green), tightly masked (red), and corrected (purple).

(C) Angular distribution of the particles used for the final reconstruction of the major class.

(D) A superposition between the caspase-1/pro-IL-18 and the caspase-4/pro-IL-18 complexes. The caspase-1/pro-IL-18 complex (color code consistent with that in Fig. 3E-F) and the caspase-4/pro-IL-18 complex (PDB: 8SPB, in gray) are overlaid at the caspase region with a backbone heavy atom RMSD of 0.54. Pro-IL-18 molecules in the caspase-4 complex appear to be a bit more closed than those in the caspase-1 complex.

A Crosslinked lysine pairs between caspase-1 p10 and pro-IL-18

Caspase-1 p10	Pro-IL-18	Ca-Ca (Å)
317-AIKKA-321	40-KLESKLSVIRN-50	22.9
317-AIKKA-321	93-RGMAVTISVKCEKI-107	11.6
317-AIKKA-321	140-RSVPGHDNKMQFES SSYEGYFLACEKE-166	18.6
317-AIKKA-321	167-RDLFKLILKK-176	23.6
319-KKAHIEKD-326	17-KFIDNTLYFIAEDDENL ESDYFGKLESKL-45	19.8
319-KKAHIEKD-326	40-KLESKLSVIRN-50	16.1
319-KKAHIEKD-326	140-RSVPGHDNKMQFES SSYEGYFLACEKE-166	15.3

C Crosslinked lysine pairs between caspase-1 p20 and pro-IL-18

Caspase-1 p20	Pro-IL-18	Ca-Ca (Å)
246-KKHSEQVPDILQLNAI FNMLNTKNCPSLKD-275	140-RSVPGHDNKMQFES SSYEGYFLACEKE-166	12.9
259-RGDSPGVVWFKD-270	40-KLESKLSVIRN-50	22.2
259-RGDSPGVVWFKD-270	140-RSVPGHDNKMQFES SSYEGYFLACEKE-166	16.6
259-RGDSPGVVWFKD-270	167-RDLFKLILKK-176	18.0
259-RGDSPGVVWFKD-270	171-KLILKE-177	22.2

E Crosslinked lysine pairs within pro-IL-18, in caspase-1/pro-IL-18 complex

Pro-IL-18	Pro-IL-18	Ca-Ca (Å) in complex / IL-18
40-KLESKLSVIRN-50	148-KMQFESSSYEGYFLA CEKERD-168	18.7 / 33.6 Too far in IL-18
40-KLESKLSVIRN-50	171-KLILKE-177	13.8 / 31.9 Too far in IL-18

All the remaining pairs are consistent with structures of both the caspase-1/pro-IL-18 complex and mature IL-18 (PDB: 3WO2).

G One pro-IL-18 molecule binds

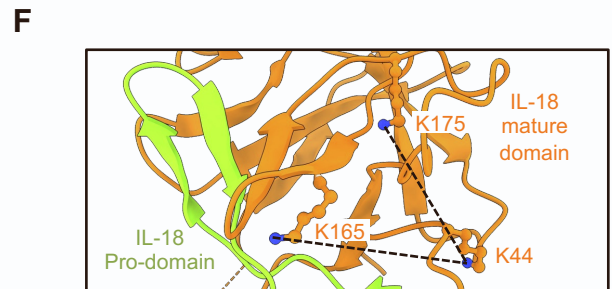
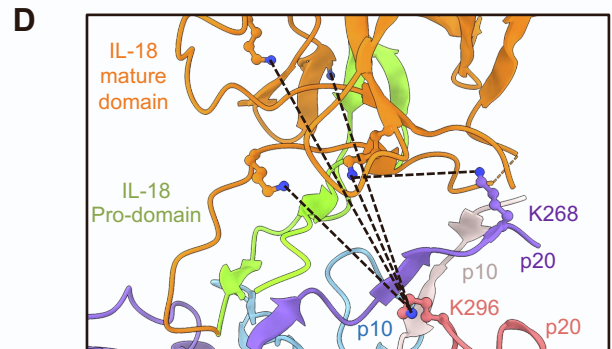
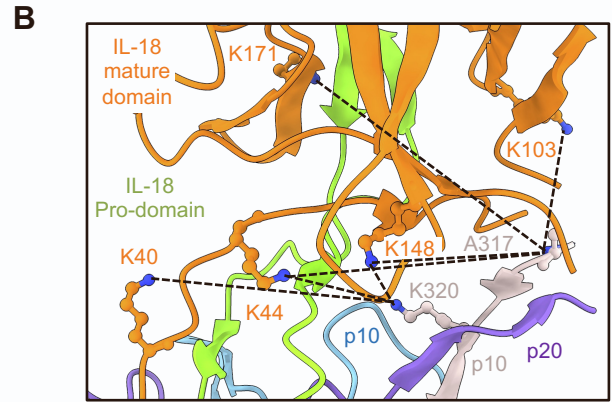
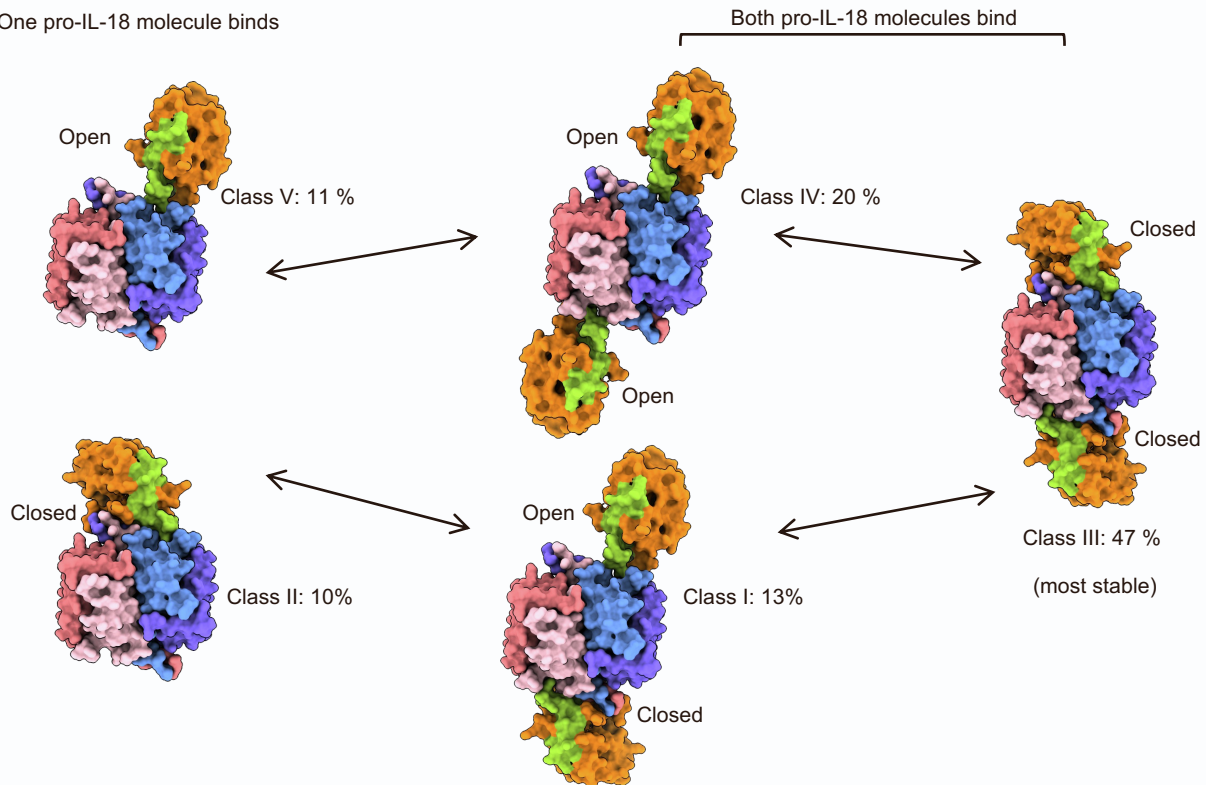


Figure S5. Crosslinking mass spectrometry analysis of caspase-1/pro-IL-18, and variable modes of recognition of pro-IL-18 by caspase-1, related to Figure 3

(A-B) Summary of BS3 crosslinked lysine pairs between caspase-1 p10 and pro-IL-18. The crosslinked peptides with high confidence are shown with residue ranges in their domain colors (A), and on the structure with black dotted lines (B).

(C-D) Summary of BS3 crosslinked lysine pairs between caspase-1 p20 and pro-IL-18. The crosslinked peptides with high confidence are shown with residue ranges in their domain colors (C), and on the structure with black dotted lines (D).

(E-F) Summary of BS3 crosslinked lysine pairs within pro-IL-18 in the caspase-1/pro-IL-18 complex. The crosslinked peptides with high confidence are shown with residue ranges in their domain colors (E), and on the structure with black dotted lines (F).

(G) Variable modes of recognition of pro-IL-18 by caspase-1 that involve only the active site or both the active site and the exosite. Presumably, both open and closed modes of interaction can result in pro-IL-18 processing by caspase-1.

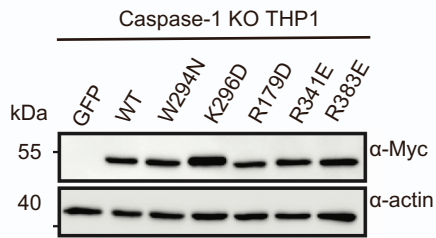
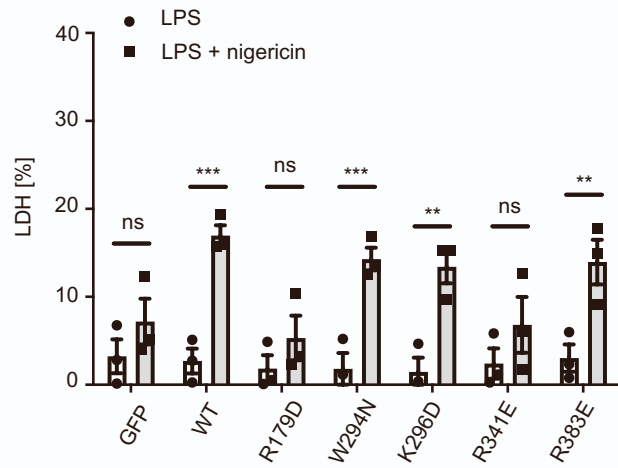
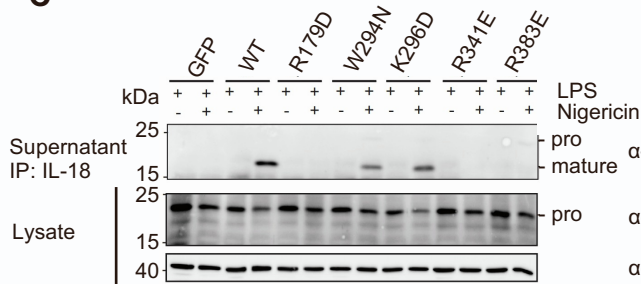
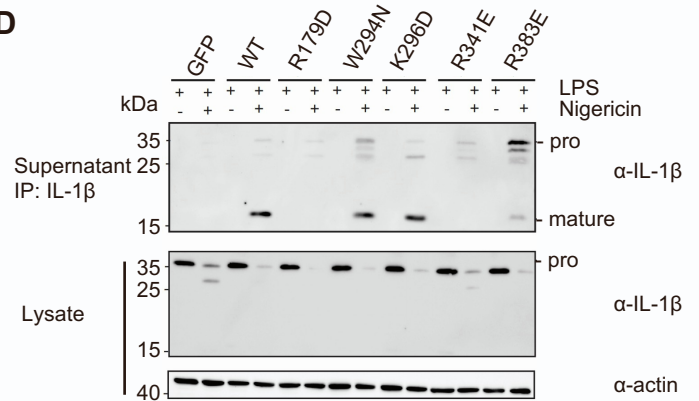
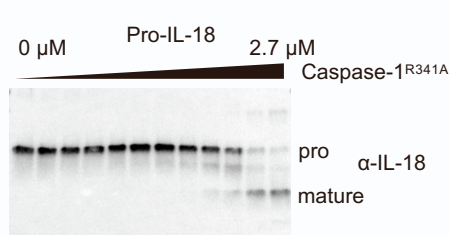
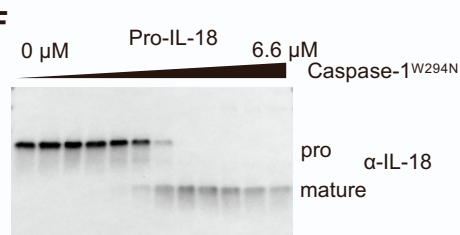
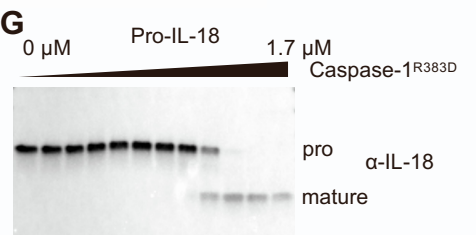
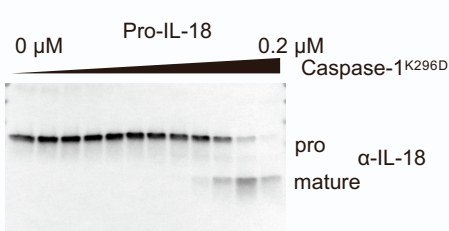
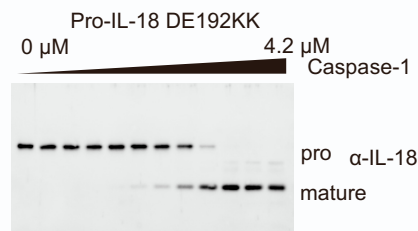
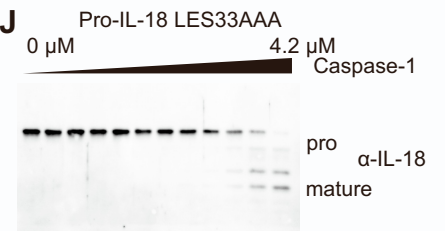
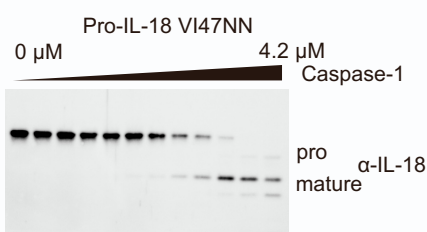
A**B****C****D****E****F****G****H****I****J****K**

Figure S6. Mutations of key residues at the two interfaces impair the binding and cleavage of pro-IL-18 and pro-IL-1 β by caspase-1, related to Figure 4 and 5

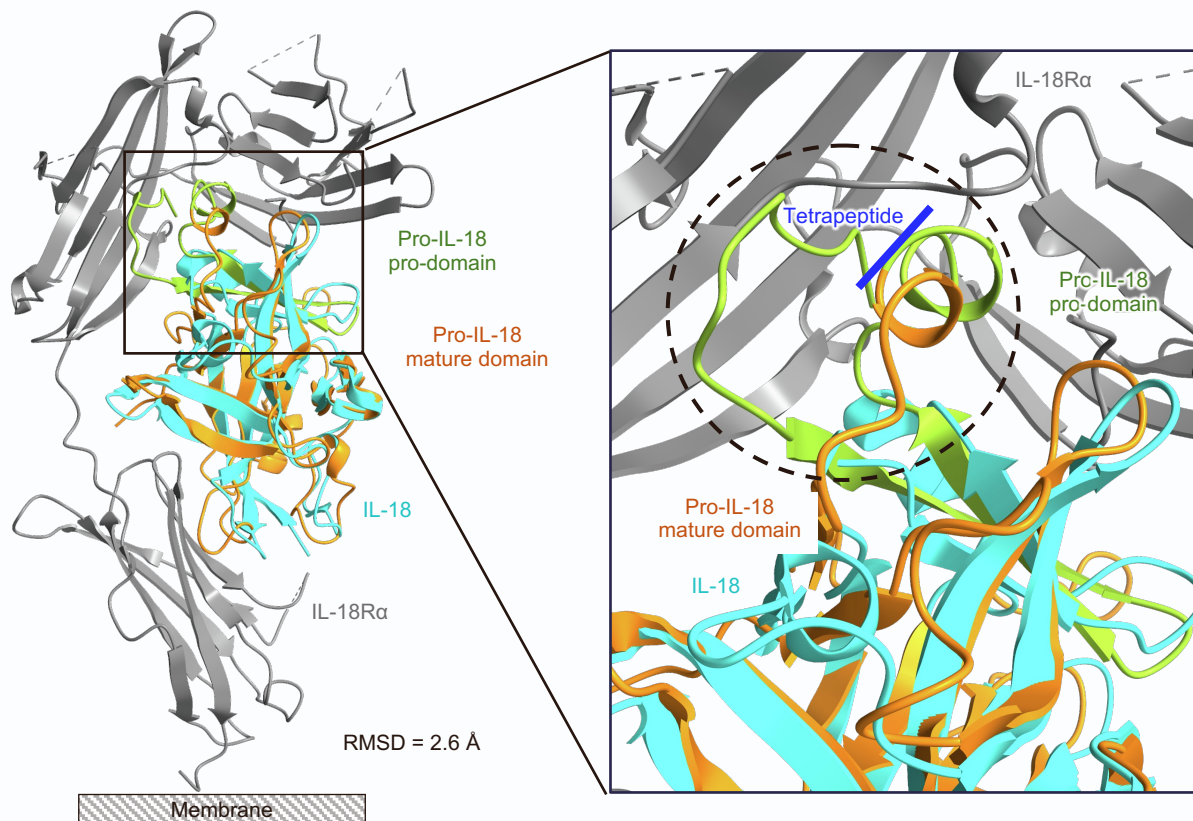
(A) Immunoblot showing stable expression of the indicated, Myc-tagged caspase-1 mutants in *CASP1*^{-/-} THP-1 cells.

(B) LDH release from *CASP1*^{-/-}KO THP-1 macrophages expressing indicated caspase-1 mutants primed with LPS for 4 h, or also followed by nigericin stimulation for 3 h.

(C,D) Caspase-1-deficient THP-1 macrophages reconstituted with indicated caspase-1 mutants primed with LPS for 4 h before treatment with nigericin for 2-3 h. IL-18 (C) and IL-1 β (D) were immunoprecipitated from cell culture supernatants and analyzed by immunoblot.

(E-K) Immunoblots showing *in vitro* cleavage of WT and mutant pro-IL-18 by WT and mutant caspase-1. Specific mutants used are indicated. The concentrations displayed are active caspase-1 concentrations determined by active site titration assay, and are 2-fold dilution series.

The data shown are representative of three independent experiments. Bars and error bars represent the mean \pm SEM of at three independent experiments. Statistical significance was determined by two-way ANOVA with Tukey's multiple comparisons test: **p < 0.01; ***p < 0.001.

A**B**

IL-18/IL-18BP complex (7AL7)

Pro-IL-18 superimposed with IL-18/IL-18BP complex (7AL7), pro-IL-18 is shown

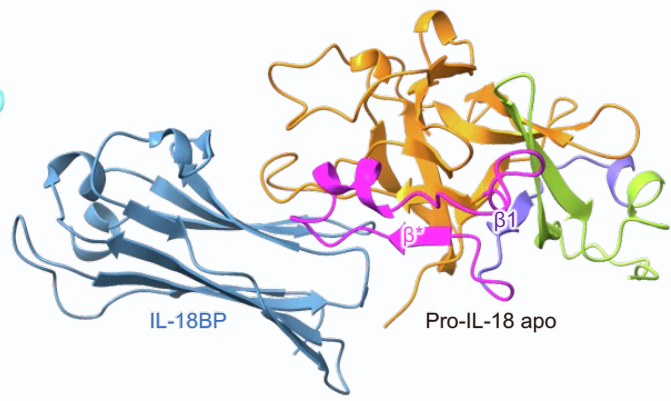
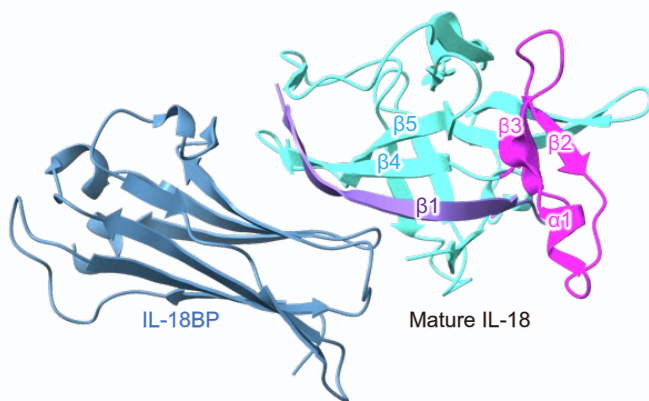


Figure S7. Pro-IL-18 and mature IL-18 structures, related to Figure 7

(A) Overlay of pro-IL-18 onto the IL-18/IL-18R α complex structure (PDB: 4R6U), showing the steric hindrance to receptor binding by the tetrapeptide motif region of pro-IL-18. The color code for the domains is consistent with that in Figure 7.

(B) The comparison of pro-IL-18 and mature IL-18 for IL-18BP binding. Pro-IL-18 apo is aligned with IL-18 in the IL-18/IL-18BP complex (7AL7). The $\beta 2$ - $\beta 3$ - $\alpha 1$ region (magenta) in mature IL-18 rearranged from β^* and the following region in pro-IL-18 apo is not involved in the binding (left). The β^* and the following region in pro-IL-18 clash with IL-18BP binding. The short $\beta 1$ in pro-IL-18 apo changes into the long $\beta 1$ in mature IL-18 to mediate the interaction with IL-18BP. The color code for the domains is consistent with that in Figure 7.

Table S1. Data Collection, processing and validation statistics, related to Figure 3

Data Collection and Processing	
Microscope	Titan Krios
Voltage (keV)	300
Camera	K3
Magnification	105,000
Pixel size at detector (Å/pixel)	0.83
Total electron exposure (e ⁻ /Å ²)	55.4
Exposure rate (e ⁻ /pixel/sec)	12.7
Number of frames collected during exposure	40
Defocus range (µm) (0° / 30° tilt angle)	-1.0 to -2.5 / -0.8 to -1.8
Automation software	SerialEM 3.8
Energy filter slit width (eV)	20
Micrographs collected (no.) (0° / 30° tilt angle)	4,437 / 3,240
Micrographs used (no.) (0° / 30° tilt angle)	4,377 / 2,459
Total extracted particles (no.) (0° / 30° tilt angle)	4,218,303 / 2,881,641
Refinement	
Refined particles (no.) / Final particles (no.)	440,340 / 206,959
Symmetry parameters	C2
Map resolution (Å)	3.5
FSC 0.143 (unmasked / masked)	3.5 / 4.4
Resolution range (Å)	3.2 to 8.8
Resolution range due to anisotropy (Å)	3.4 to 4.0
Map sharpening <i>B</i> factor range (Å ²)	-165.1
Map sharpening methods	LocalDeblur
Model composition	
	6
Chains	792
Protein residues	
Validation	
Model-Map scores	
CC (correlation coefficients)	0.71
Average FSC (0 / 0.143 / 0.5)	2.7 / 3.5 / 4.2
R.m.s. deviations from ideal values	
Bond lengths (Å)	0.003
Bond angles (°)	0.755
MolProbity score	1.96
CaBLAM outliers	3.82
Clashscore	10.35
Poor rotamers (%)	0.7
C-beta outliers (%)	0.00
Ramachandran plot	
Favored (%)	93.43
Allowed (%)	6.19
Outliers (%)	0.39

Table S2. Summary of NMR structural statistics for pro-IL-18^a, related to Figure 6

Parameters		
Completeness of resonance assignments ^b		
Backbone (%)		99.3
Side chain (%)		96.9
Aromatic (%)		97.8
Stereospecific methyl (%)		95.2
Conformationally-restricting restraints		
Distance restraints		
Total		4053
Intra-residue (i = j)		859
Sequential (i-j = 1)		1030
Medium range (1 < i - j < 5)		509
Long range (i - j ≥ 5)		1655
Dihedral angle restraints		
Total		136
φ + ψ		124
χ ¹		12
No. of restraints per residue		21.9
No. of long-range restraints per residue		8.7
Residual restraint violations ^c		
Average no. of distance violations per structure:		
0.1 - 0.2 Å		13.0
0.2 - 0.5 Å		11.1
> 0.5 Å		8.5
average RMS distance violation / constraint (Å)		0.34
Maximum distance violation (Å)		1.16
Average no. of dihedral angle violations per structure:		
1 - 10°		3.7
> 10°		0.1
average RMS dihedral angle violation / constraint (degree)		4.45
Maximum dihedral angle violation (°)		11.3
Model Quality		
RMSD backbone atoms (Å) ^d		0.50
RMSD heavy atoms (Å) ^d		0.73
RMSD deviation of bond lengths (Å)		0.010
RMSD deviation of bond angles (°)		0.3
No. of close contacts		4
MolProbity Ramachandran statistics ^d		
Most favored regions (%)		97.0
Additionally allowed regions (%)		2.9
Disallowed regions (%)		0.2
Global quality scores	Raw score	Z-score
Procheck (phi-psi) ^d	-0.32	-0.94
Procheck (all) ^d	-0.09	-0.53
MolProbity clash score	8.51	0.07

^a Structural statistics were computed using PSVS 2.0⁶⁰ and PDBStat 5.23.08.⁵⁹

^b Calculated from the total expected number of peaks excluding highly exchangeable protons (N-terminal, Lys, and Arg amino groups, hydroxyls of Ser, Thr, and Tyr, free thiols of Cys, carboxyls of Asp and Glu, and non-protonated aromatic carbons).

^c Average distance violations were calculated using sum over r^6 .

^d Calculated for ordered residue ranges based on ¹⁵N relaxation data: 11-28,45-60,80-88,97-104,107-112,114-120,133-145,147-165,170-179,185-190.